Publications of the Astronomical Society of Australia (2022), 1–22
doi:XX.XXXX/pasa.XXXX.XX

CAMBRIDGE
UNIVERSITY PRESS

RESEARCH PAPER

The Southern-sky MWA Rapid Two-metre (SMART) pulsar survey - II. Survey status, pulsar census, and first pulsar discoveries

N. D. R. Bhat,[1] N. A. Swainston,[1] S. J. McSweeney,[1] M. Xue,[2] B. W. Meyers,[1,3] S. Kudale,[4] S. Dai,[5] S. E. Tremblay,[6] W. van Straten,[7] R. M. Shannon,[8] K. R. Smith,[1] M. Sokolowski,[1] S. M. Ord,[9] G. Sleap,[1] A. Williams,[1] P. J. Hancock,[10] R. Lange,[10] J. Tocknell,[11] M. Johnston-Hollitt,[10] D. L. Kaplan,[22] S. J. Tingay,[1] and M. Walker[1]

[1]International Centre for Radio Astronomy Research, Curtin University, Bentley, WA 6102, Australia
[2]National Astronomical Observatories, Chinese Academy of Sciences, Datun Road, Chaoyang District, Beijing 100101, China
[3]Department of Physics & Astronomy, University of British Columbia, 6224 Agricultural Road, Vancouver, BC V6T 1Z1, Canada
[4]National Centre for Radio Astrophysics, Tata Institute of Fundamental Research, Pune 411 007, India
[5]Western Sydney University, Locked Bag 2751, Penrith South DC, NSW 1797, Australia
[6]National Radio Astronomy Observatory, 1003 Lopez Road, Socorro NM, 87801, USA
[7]Institute for Radio Astronomy & Space Research, Auckland University of Technology, Private Bag 92006, Auckland 1142, New Zealand
[8]Centre for Astrophysics and Supercomputing, Swinburne University of Technology, P.O. Box 218, Hawthorn, VIC 3122, Australia
[9]CSIRO Astronomy and Space Science, PO Box 76, Epping, NSW 1710, Australia
[10]Curtin Institute for Computation, Curtin University, GPO Box U1987, Perth, 6845, WA, Australia
[11]AAO Macquarie, Macquarie University, NSW, Australia
[22]Department of Physics, University of Wisconsin–Milwaukee, WI 53201, USA

(Received dd Mmm YYYY; revised dd Mmm YYYY; accepted dd Mmm YYYY; first published online dd Mmm YYYY)

Abstract

In Paper I, we presented an overview of the Southern-sky MWA Rapid Two-metre (SMART) survey, including the survey design and search pipeline. While the combination of MWA's large field-of-view and the voltage capture system brings a survey speed of $\sim$450 deg^2 hr^{-1} , the progression of the survey relies on the availability of compact configuration of the Phase II array. Over the past few years, by taking advantage of multiple windows of opportunity when the compact configuration was available, we have advanced the survey to 75% of the planned sky coverage. To date, about 10% of the data collected thus far have been processed for a first-pass search, where 10 min of observation is processed for dispersion measures out to 250 pc cm^{-3}, to realise a shallow survey that is largely sensitive to long-period pulsars. The ongoing analysis has led to two new pulsar discoveries, as well as an independent discovery and a rediscovery of a previously incorrectly characterised pulsar, all from $\sim$3% of the data for which candidate scrutiny is completed. In this sequel to Paper I, we describe the strategies for further detailed follow-up including improved sky localisation and convergence to timing solution, and illustrate them using example pulsar discoveries. The processing has also led to re-detection of 120 pulsars in the SMART observing band, bringing the total number of pulsars detected to date with the MWA to 180, and these are used to assess the search sensitivity of current processing pipelines. The planned second-pass (deep survey) processing is expected to yield a three-fold increase in sensitivity for long-period pulsars, and a substantial improvement to millisecond pulsars by adopting optimal de-dispersion plans. The SMART survey will complement the highly successful Parkes High Time Resolution Universe survey at 1.2-1.5 GHz, and inform future large survey efforts such as those planned with the low-frequency Square Kilometre Array (SKA-Low).

Keywords: surveys: sky surveys – instrumentation: interferometers – methods: observational – pulsars: general – techniques: interferometric

1. INTRODUCTION

Large pulsar surveys have played a pivotal role in advancing pulsar astronomy. They have collectively led to a substantial increase in the population of known pulsars (e.g., Manchester et al., 1978, 2001; Han et al., 2021), with the discoveries of exotic objects (e.g., the double pulsar, the transitional millisecond pulsar) leading to transformational science (e.g., Lyne et al., 2004; Kramer et al., 2021; Archibald et al., 2009). As such, conducting a full Galactic census and exploiting the specialised targets for high-profile science, such as testing strong-field gravity and detecting nanohertz-frequency gravitational waves, is a headline science theme for the Square Kilometre Array (SKA) and many of its precursor and pathfinder facilities (Keane et al., 2015; Shao et al., 2015; Janssen et al., 2015; Bailes et al., 2020).

The radically new designs of next-generation facilities bring significant changes (as well as challenges) to the pulsar survey landscape. For instance, all-sky surveys, which have been mainly a single-dish arena for long, will now have to be conducted using distributed interferometric arrays or aperture arrays that make up these new generation facilities such as the Low Frequency Array (LOFAR; van Haarlem et al. 2013) and the Murchison Widefield Array (MWA; Tingay et al. 2013; Wayth et al. 2018). They present a substantial complexity given the inherent beamforming cost and large data rates, but also provide the benefits of significantly larger survey speeds, and new avenues for candidate confirmation and follow-up. At frequencies below 300 MHz, the ongoing LOFAR Tied-Array All-Sky (LOTAAS; Sanidas et al. 2019) survey is the first such major step, while the South African MeerKAT telescope is proving to be highly successful in sensitive targeted searches (e.g., Ridolfi et al., 2022). In the first paper of this series (hereafter referred to as Paper I), we described the Southern-sky MWA Rapid Two-metre (SMART) survey, a large project to

search for pulsars and fast transients with the MWA's 140–170 MHz band, in the entire sky south of +30°in declination.

While there has been substantial progress in terms of data collection effort, the SMART survey is currently in its early stages in terms of data processing and analysis. The adoption of voltage recording for survey data collection requires full-scale tied-array beamforming as the front-end of the processing chain, but it offers a number of unique benefits for candidate follow-up and confirmation. Most notably, the SMART survey has minimal reliance on new observations for immediate follow-up and/or confirmation of pulsar candidates. Access to the voltage data even allows accurate positional determination through a dense-grid localisation, using either survey data alone, or in combination with archival data, as vividly demonstrated in Paper I (see also Swainston et al., 2021) through examples from early discoveries.

Nevertheless, scientific merits of most new pulsar discoveries are typically revealed in due course of time, often through targeted follow-ups using more sensitive telescopes, or long-term timing observations. Two important pre-requisites are: 1) an accurate sky position, and 2) a full coherent timing solution. The latter typically relies on a series of regular observations carried out over the course of time. Again, with the advent of sensitive high-resolution imaging instruments such as the upgraded Giant Metre-wave Radio Telescope (uGMRT; Gupta et al., 2017), and large survey data releases from sensitive imaging facilities such as the Australian SKA Pathfinder (ASKAP; McConnell et al., 2020), source identification and localisation can be expedited for arc-second level positional determination early on, thereby accelerating convergence to an initial timing solution. The design of the SMART also offers additional benefits, by virtue of its overlapping pointings, as detailed in Paper I. Moreover, when archival data are available, they can be utilised for an investigation of source variability, or for extending timing analysis, as demonstrated in Swainston et al. (2021).

In Paper I, we described the survey design, science goals, current processing pipelines and follow-up strategies. In this sequel to Paper I, we present the survey status and further details on the initial discoveries, demonstrate and verify some of the detailed follow-up strategies, and provide a brief census of pulsar re-detections. In § 2, we present the survey status, and in § 3 details on confirmation and follow-up. Initial pulsar discoveries are summarised in § 4, where we also present re-detections of a large sample of previously known pulsars from our SMART data processing. A summary is presented in § 5.

2. Survey Status

Even though the use of the voltage capture system (VCS) and the MWA's large field-of-view (FoV) means the data collection part of the survey can be completed in <100 hours of telescope time, practical considerations such as the data rate (42 TB per observation) and the availability of the compact configuration necessitate that the survey be carried out in multiple observing campaigns. By taking advantage of such windows of opportunity in the past few years, we have advanced the data collection effort to 75%. Specifically, through four dedicated campaigns in the 2018B, 2019B, 2020A and 2021A semesters, we have covered much of the sky within the right ascension (RA) range <16 hr and >21 hr and declination south of +30°, as shown in Fig. 1. The fourth campaign to cover the 13-17 hr RA range was only partially complete, as the system was no longer available for observations for an extended period since May 2021. Further details of the pointings and observing campaigns are summarised in Table 1. The remaining 25% of the survey will be undertaken once the array returns to the compact configuration (by around mid-2023). Substantial progress has already been made with the science commissioning of the new corelator/voltage capture system (MWAX VCS), with the successful demonstration of the ability to attain full coherent beam sensitivity.

In the ongoing first-pass search, 10 min of data from each observation are processed in 2358 trial dispersion measures (DMs) out to 250 pc cm^{-3}, thus effectively performing a shallow survey of a large part of the southern sky. The limiting sensitivity achieved is comparable, or slightly better than, that of the Parkes 70cm survey from the 1990s (Manchester et al., 1996), at least for pulsars with spectral index $\alpha \lesssim -1.6$. At the time of writing, processing is completed for $\sim$10% of the data collected thus far, covering $\sim$55% of the sky searched in the *shallow survey* phase, resulting in $\sim$1 million candidates, after filtering through the current machine-learning (ML) tools. Efforts are under way to substantially improve the efficacy of candidate filtering schemes, using semi-supervised generative adversarial network (SGAN) based classifiers (e.g., Balakrishnan et al., 2021), and will be integrated into the processing pipelines in the near future. Initial results are encouraging, and details including current implementation and the efficacy achieved, will be described in a future publication.

The current efficacy of ML tools means that a large volume of candidates require human scrutiny; however, only a small fraction ($\lesssim$3%) of these have been examined for promising candidates to follow-up, resulting in four pulsar discoveries, including an independent discovery and a re-discovery of a previously incorrectly characterised pulsar, as well as re-detections of 120 previously known pulsars. All four discoveries have been followed up with Parkes and uGMRT, and also using archival/new data from the MWA, for early science extraction, and with the intent to develop and demonstrate effective follow-up strategies. Detection plots of PSRs J1002–2036 and J1357–2530 are shown in Fig. 2. The parameters of the three new pulsars are summarised in Table 2, and some of their detailed characteristics are described in the sections below.

3. Follow-up of pulsar discoveries

As described in Paper I, the SMART survey's unique design offers a range of flexible reprocessing avenues for candidate confirmation and improved positional determination, without having to rely on making immediate new observations. Furthermore, the archival data from past VCS projects can be leveraged for further detailed follow-up and characterisation, as demonstrated in Swainston et al. (2021) and McSweeney

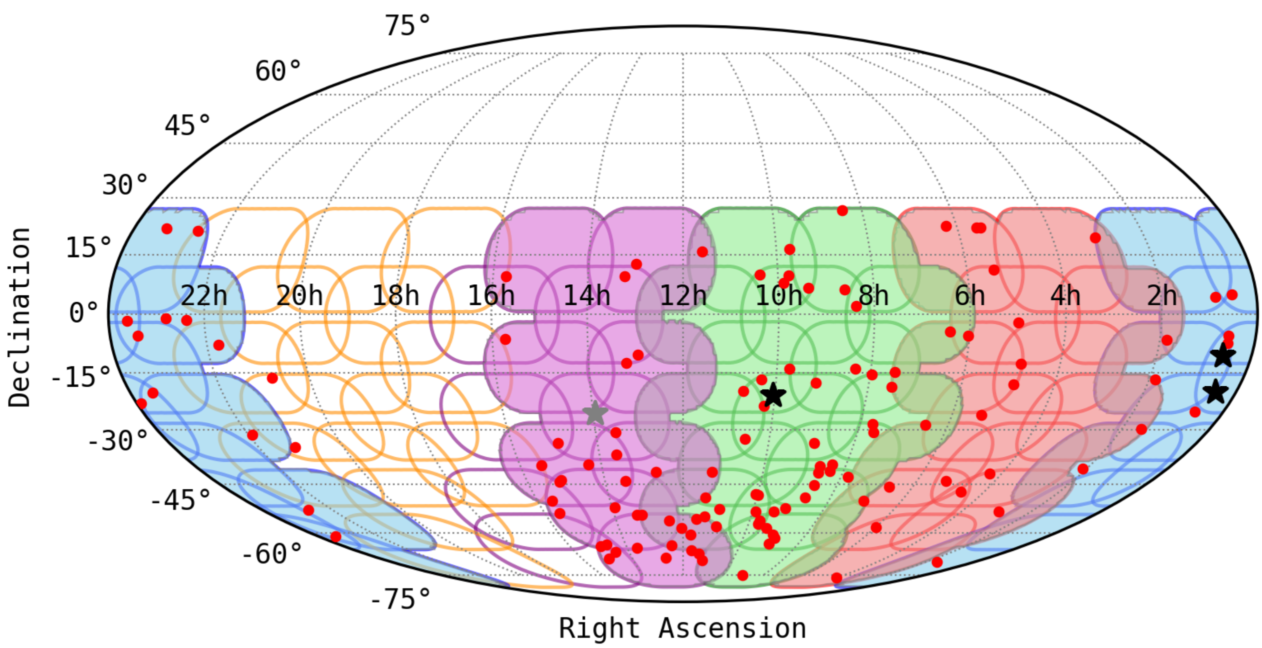


Figure 1. Sky plot summarising the observing strategy adopted for the SMART pulsar survey and the progress made to date: the full visible sky (i.e., declination < $+30^{\circ}$) is covered using 70 pointings that overlap 10° in LST and 15° in declination. The coloured contours represent the half-power points of the main lobe of the tile (primary) beam (at 155 MHz). The blue, red, and green pointing sets, as well as 10 of the 13 purple ones, have already been observed through four dedicated observing campaigns undertaken in the 2018B, 2019B, 2020A, 2021A semesters. The red filled circles are the known pulsar detections from the survey data (120 so far), and the black stars are the three new pulsar discoveries, including PSR J0026–1955, an independent discovery from the SMART. The grey star is PSR J1357–2530, a re-discovery of a previously incorrectly characterised pulsar.

Table 1. Summary of the survey observing campaigns to date

Observing semester	Dates of observation	No. of VCS pointings	RA range (hr)	Data collected (TB)	Completion status (%)	Redetected pulsars†
2018B	September - December 2018	13	22-3	546	100	24
2019B	September - November 2019	13	2-7	546	100	23(3)
2020A	January - March 2020	15	6-12	630	100	58(2)
2020B	April - May 2021	10	12-16	420	75	31(7)

† The number in parentheses are common redetections with the previous semester; e.g., 3 pulsars were detected in both 2018B and 2019B observations.

Table 2. Parameter summaries of SMART pulsar discoveries

Parameter	PSR J0036–1033	PSR J0026–1955[1]	PSR J1002–2036	PSR J1357–2530[2]
Right ascension (J2000)	$00^h36^m15^s.01(4)$	$00^h26^m36^s.3(2)$	$10^h02^m39^s.3$	13^h57^m24s
Declination (J2000)	$-10^{\circ}33'14''.2(9)$	$-19^{\circ}55'59''.3(30)$	$-20^{\circ}44'41''.4$	$-25^{\circ}30'39''$
Galactic longitude (l)	112.3°	87.3°	258.7°	321.16°
Galactic latitude (b)	–72.9°	–80.9°	27.3°	35.02°
Spin period (P)	0.900009289(3) s	1.30615183533(1) s	1.677733 s	0.912 s
Dispersion measure (DM)	23.1(2) $\mathrm{pc\,cm^{-3}}$	20.81(1) $\mathrm{pc\,cm^{-3}}$	43.282 $\mathrm{pc\,cm^{-3}}$	16.046 $\mathrm{pc\,cm^{-3}}$
Flux density at 400 MHz	1 mJy	4.2 mJy	–	0.5-1 mJy
Flux density at 1400 MHz	0.1 mJy	0.3 mJy	0.1 mJy	–
Spectral index (α)	-2.0 ± 0.2	-1.6	$\lesssim -2$	–
Rotation measure (RM)	$-8.1 \pm 0.7\ \mathrm{rad\,m^{-2}}$	$3.65 \pm 0.09\ \mathrm{rad\,m^{-2}}$	–	

[1] Independent rediscovery. The source was first detected as a GBNCC candidate (cf. McSweeney et al., 2022). A full timing solution from MWA data is presented in Table 4.
[2] Independent rediscovery of a previously incorrectly characterised pulsar. See text (§ 4.1.4) for details.

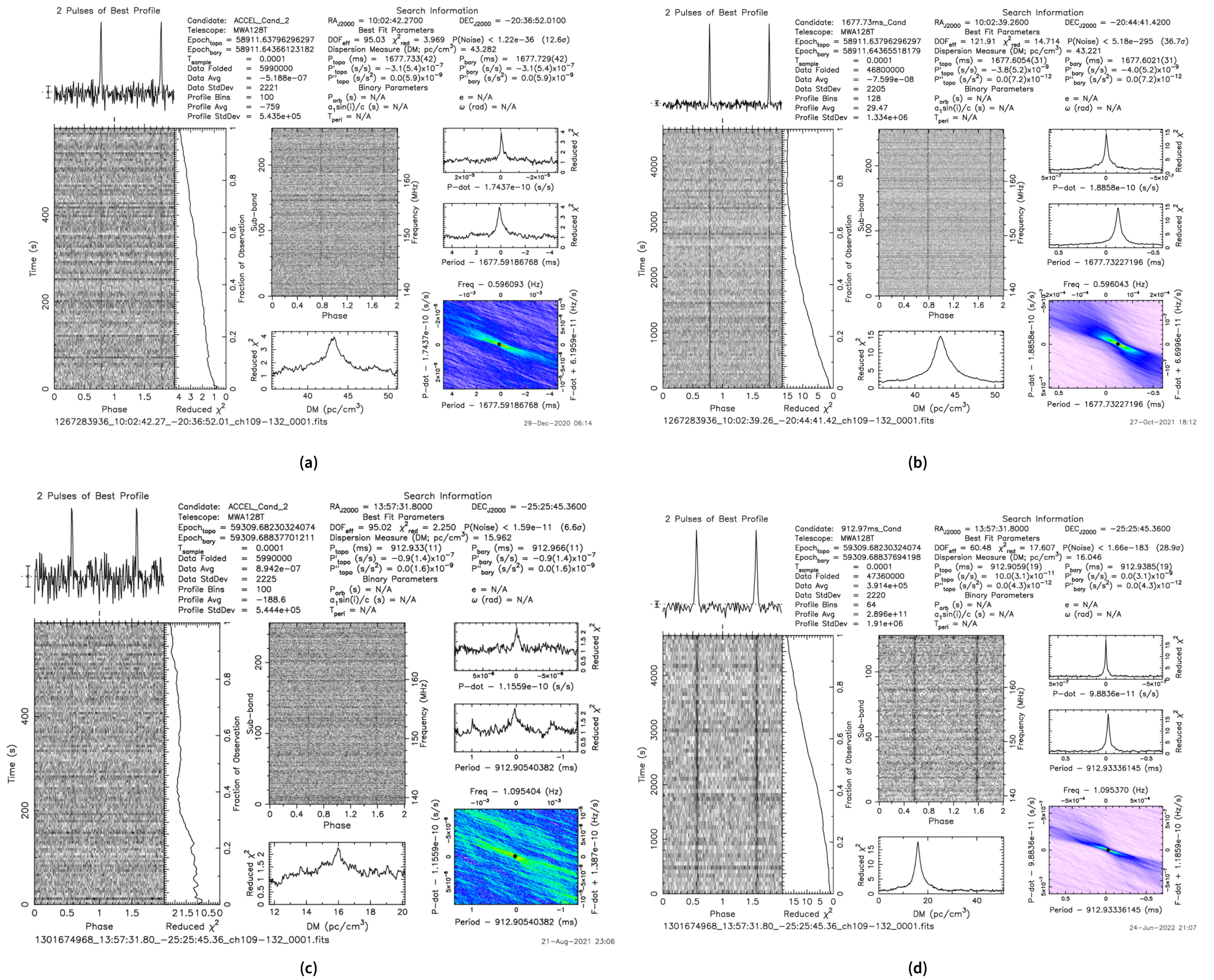


Figure 2. Detection plots of PSRs J1002–2036 and J1357–2530 from SMART search processing. Panels (a) and (c) are diagnostic plots (from PRESTO) of the original candidate detections (PSR J1002–2036 and PSR J1357–2530, respectively), while panels (b) and (d) show the improved detections from follow-up processing (confirmation) using the same inital detection observation, but by forming a tied-array beam for the full 80-min observing duration.

et al. (2022); e.g., extending an initial timing solution derived from regular observations to determine the spin period (P) and its first time-derivative ($\dot{P}$). An improved sky position is vital for follow-ups with more sensitive telescopes operating at higher frequencies, but a convergence toward this can be expedited via high-resolution imaging using facilities such as the uGMRT.

In the following sections we outline some additional strategies that are natural extensions to those already described in Paper I. These include: (1) an interferometric localisation via high-resolution imaging, (2) the processing of archival VCS observations for an extended timing analysis, and (3) high-frequency follow-up using sensitive telescopes such as the uGMRT and Parkes. As we have demonstrated in earlier publications from the SMART survey, some of these are proving useful for rapid convergence to a working pulsar timing solution (e.g., Swainston et al., 2021), and for ascertaining the detailed characteristics in terms of scientific significance (e.g., McSweeney et al., 2022).

3.1 Imaging for improved localisation

3.1.1 High resolution imaging with the uGMRT

Beyond the tied-array beam localisation as detailed in Paper I, the position of SMART-discovered pulsars can be further improved via high-resolution continuum imaging with interferometric arrays, for which the high sensitivity and angular resolution of the upgraded GMRT (uGMRT) is highly appealing, provided the source is north of −55° in declination, and the spectrum is not ultra-steep (spectral index, $\alpha \gtrsim -3$). For PSR J0036–1033, the first discovered MWA pulsar, this was convincingly demonstrated in Swainston et al. (2021), for which the localisation uncertainty was significantly improved

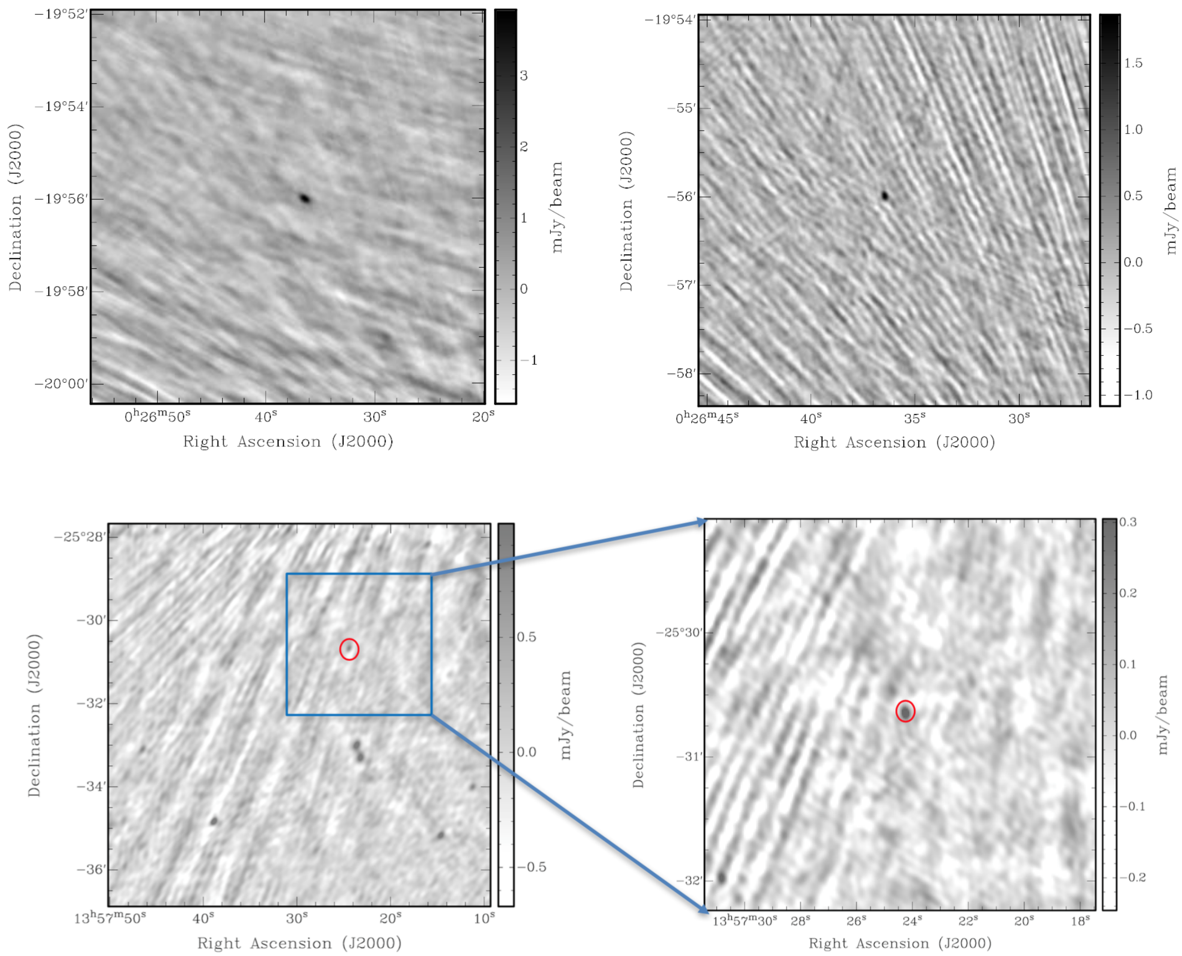


Figure 3. *Upper panels*: uGMRT images of PSR J0026–1955 in Band 3 (300-500 MHz; *left*) and Band 4 (550-750 MHz; *right*), obtained from integration times of 136 min and 56 min, respectively. The rms sensitivity is $\approx$276 μJy beam^{-1} in Band 3, and $\approx$210 μJy beam^{-1}, respectively, yielding $\sim 15\sigma$ and $\sim 10\sigma$ detection of the pulsar. The presence of a bright nearby source (4 Jy at 400 MHz, at $\sim 10.5'$ from the pulsar position) impacts the quality of calibration achievable, as seen in Band 4 observations. Band 3 observations were made at an offset position of the pulsar, and the effect of the bright source was subdued owing to attenuation of the primary beam. *Lower panels*: uGMRT images of PSR J1357–2530 in Band 3 (300-500 MHz; *left*) and Band 4 (550-750 MHz; *right*), obtained from integration times of 90 min and 71 min, respectively. The rms sensitivity is $\approx$153 μJy beam^{-1} in Band 3, and $\approx$53 μJy beam^{-1}, respectively, yielding $\sim 6\sigma$ and $\sim 11\sigma$ detection of the pulsar. Band 3 imaging of the initial (poorly localised) pulsar position revealed multiple compact sources, one of which turned out to be the pulsar (see § 4.1.4 for details).

Table 3. Localisation summary of PSR J0026–1955

Telescope/System	Method	Right Ascension (J2000)	Declination (J2000)
MWA VCS	Tied-array beams	$00^h26^m37.5^s$	$-19°56'24.9''$
uGMRT Band 3	Imaging	$00^h26^m36.2^s$	$-19°55'59.6''$
uGMRT Band 4	Imaging	$00^h26^m36.41^s$	$-19°55'59.0''$
Final position	Imaging	$00^h26^m36^s.3(2)$	$-19°55'59''.3(30)$

from an initial $\sim 10'$ (i.e., discovery observation) to $\sim 10''$ through a dense-grid tied-array beam (TAB) localisation using the three different array configurations, and then eventually to $\lesssim 1''$ via high-resolution imaging of the pulsar using uGMRT Band 3 and 4 (300–750 MHz) observations.

For PSR J0026–1955, even though uGMRT observations were made in similar bands using the identical setup (i.e., concurrent visibility recording and phased-array beams), and analysed using similar procedures, imaging of Band 3 data (300–500 MHz) proved difficult due to the presence of a bright source ($S_{400} \sim 4$ Jy) in the vicinity ($\sim 10.5'$ from the putative pulsar position). Fortunately, our earlier observations that were made as part of the DDTC185 project (and before the realisation that the original detection was in fact through one of the grating lobes), provided significant attenuation of the source owing to the initial $\sim 42'$ (and hence incorrect) position.

Analysis of these observations resulted in a $\sim 15\sigma$ detection, as shown in the left panel of Fig. 3, notwithstanding the fact that the pulsar was at more than half-power beam width offset from the phase centre. The resultant rms of 276 μJy beam^{-1} is nearly a factor of two larger than that was achieved with the imaging analysis of PSR J0036–1033.

The imaging of Band 4 data (550–750 MHz) benefited from a much narrower primary beam (and hence a substantially higher attenuation toward the bright, nearby source), besides a reduced flux density due to spectral index, yielding a $\sim 10\sigma$ detection of the pulsar, as shown in the right panel of Fig. 3. The rms attained in this case is ≈ 210 μJy beam^{-1}, almost an order of magnitude larger than that is typically attainable for deep imaging of 1 hr in uGMRT Band 4. This illustrates the complexity in interferometric localisation, when the imaging analysis is hampered by bright sources in the vicinity.

A summary of uGMRT-derived positions are given in Table 3, along with the initial MWA-derived position. There is $\approx 32''$ discrepancy between the uGMRT- and MWA-derived positions, which can be possibly attributed to a residual ionospheric refraction as discussed in Swainston et al. (2022a). It is possible that the $\approx 3''$ offset between the two uGMRT bands may also be caused by the ionosphere; even so, the final position, which we adopt as the mean of those from the two uGMRT bands, is still over an order of magnitude more precise than that reported by McSweeney et al. (2022). Further resolution to this will be possible once an improved (and fully coherent) timing solution becomes available.

3.1.2 *Imaging with the MWA*

For sources outside the uGMRT's sky ($\delta < -55°$), in principle, the recorded VCS data (if available) from long-baseline configurations of the array (Phase I or Phase II extended) can be correlated offline and imaged to verify the position obtained via the TAB localisation. However, as we demonstrated in Swainston et al. (2021), even with co-addition of multiple observations we were unable to reach a sensitivity better than ~6–8 mJy beam^{-1} (for Stokes I), and hence an imaging detection may be possible only for pulsars that are sufficiently bright ($S_{150} \gtrsim 30$ mJy). For long-period pulsars, such as PSR J0026–1955, 'on' and 'off' gated imaging may also be attempted for improved detection in imaging, though this methodology is currently under development.

3.2 *Archival observations*

Apart from the observations taken as part of the SMART campaign, the MWA archive includes many VCS observations dating back to 2014 when early pulsar and high-time resolution science observations commenced. These observations were typically parts of projects focusing on individual pulsars, so the distribution of the pointing directions across the sky is non-uniform, and some areas of the sky are not covered at all. Nevertheless, if a promising SMART candidate happens to be in an historically observed part of the sky, then the archival VCS data can be used for further confirmation of the candidate without requiring extra observations be taken.

Again we use PSR J0026–1955 as an example, whose location had fortuitously been covered by multiple previous observations. Six of these observations are included in the analysis described in McSweeney et al. (2022), but since then, more archival observations have been identified and processed, as shown in Fig. 4. Depending on the intervals between detections, their duration, and the quality of the detections themselves, such archival observations can be used to constrain otherwise hard-to-measure properties of the candidate pulsars which require long follow up campaigns, such as the flux variability due to scintillation, and their timing properties.

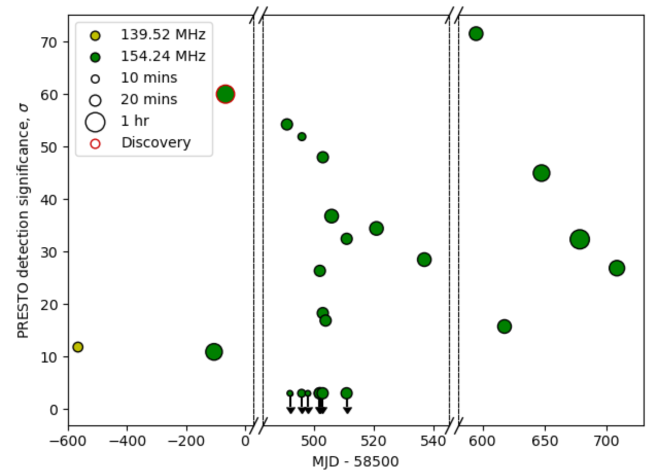


Figure 4. Detection summary of PSR J0026–1955, over a ~3.5-year time span; the PRESTO detection significance (σ) is plotted against the MJD of observation. The detection are predominantly from observations over a 30.72 MHz bandwidth centred at 154.24 MHz, with time integration varying from 10 min to 1 hr. Note that the σ reported for the discovery observation is for the full 80-minute data that was processed for follow-up and not for the 10-minute observation for initial (first-pass) search, in which the pulsar was discovered. The 3-σ upper limits indicate non-detection in a number of 10-20 min observations.

3.2.1 *Leveraging archival data to achieve timing coherence*

As an example of using the archival MWA data and improved positions from imaging follow-up (see §3.1), we are able to extract times-of-arrival (TOAs) from MWA observations alone and, in principle, phase-connect a timing solution. Here, we demonstrate that for PSR J0026–1955 across a ~1.7-year time span.

Examining the MWA VCS observation database revealed observations containing the nominal pulsar position dating back to April 2017, including dedicated followup observations for PSR J0036–1033 in late-2020 into 2021. These serendipitous observations are well suited to generating a phase-connected timing solution as there was a dense observing campaign where the same field was observed 8 times in three days (2020-10-26 to 2020-10-28), surrounded by regular observations spaced every 3-4 days for approximately 2 weeks before (2020-10-10 to 2020-10-22) and roughly weekly cadence for one month after (2020-10-30 to 2020-11-27). Monthly cadence data were then collected until the the system became unavailable for science observing (see §2). These observing

time scales are adequate to accurately determine the rotation frequency, detect spin-down and measure the DM.

The initial rotational characteristics presented by McSweeney et al. (2022) are sufficient to fold PSR J0026–1955 for a single observation, but quickly lose phase connection after ~ 1 day. Using the uGMRT imaging position (Fig. 3) and the initial estimates of the spin period and DM, we processed some of the more recent archival observations (two observations in April 2019) and the majority of the PSR J0036–1033 timing followup observations (17 observations spanning October-November 2020), creating 10-second subintegration archives with DSPSR. These archives were then subsequently processed using PSRCHIVE routines to remove RFI, specifically using the `paz` median-filtered bandpass algorithm. Since PSR J0026–1955 is a prolific nuller (cf. McSweeney et al., 2022), we manually inspected each observation with `pazi` and masked the null subintegrations to construct a high-quality average (integrated) profile. Out of the total 21 observations we processed for this work, 10 were excluded either due to non-detections (unsurprising for a pulsar with a >70% nulling fraction) or very weak detections (S/N < 15 for the fully time- and frequency-averaged profile). The five observations with the highest S/N were then combined and artificially phase aligned using `psradd` and a basic frequency-averaged template was created using `paas`, where two Gaussian components modelled the profile.

Each observation was then pre-processed such that there were four frequency subbands per epoch, from which TOAs were extracted using the `pat` utility within PSRCHIVE. The initial ephemeris used to fold the observations and the TOAs were passed to both the Tempo2 (Hobbs et al., 2006; Edwards et al., 2006) and PINT (Luo et al., 2021) pulsar timing packages. With each timing package, we were able to phase-connect all available observations to the archival data points from nearly two years earlier by updating the spin frequency, adding a spin frequency time-derivative (28σ significance), and small adjustment to the DM. Both packages produced consistent results and uncertainties. Given the sparse sampling on longer time scales we did not fit for the pulsar sky position, however, as we accrue and/or process additional observations (with the MWA or other telescopes) we will be able to constrain the position to better than the current $\sim 3''$ uncertainty obtained from the uGMRT imaging. The current best timing solution (from Tempo2) is presented in Table 4.

3.3 High-frequency follow-ups

Our ability to attain a positional accuracy of $\sim$1-2$'$ from discovery observations, or even down to $\sim$10-20$''$ when archival VCS data are also available from the long-baseline configurations of the MWA (see Paper I), facilitates high-frequency follow-ups with sensitive telescopes such as the uGMRT and Parkes that share substantial common skies with the MWA. The combination of these telescopes and their wide-band instrumentation allow nearly seamless coverage in frequency from $\sim$100 MHz to 4 GHz, thereby enabling a detailed characterisation of spectral and propagation properties of new pulsar discoveries. For instance, in the case of PSR J0036–1033, such follow-up observations helped establish the steep-spectrum ($S_\nu \propto \nu^{-2.0\pm0.2}$, where S_ν is the flux density at frequency ν) low-luminosity nature of the object (with a pseduo-luminosity $L_{1400} \sim 0.1$ mJy kpc^2 at 1400 MHz). Observational studies of this kind are an integral part of our follow-up strategies, and are important to our understanding of the Galactic pulsar population in general.

Example detections from such high-frequency follow-ups are shown in Fig. 5 for PSR J0026–1955. These were obtained using data collection and analyses procedures similar to those described in Swainston et al. (2021), i.e., concurrent imaging and phased-array observations using the uGMRT Band 3 (300-500 MHz) and Band 4 (550-750 MHz) receivers, and observations using the Parkes (*Murriyang*) telescope. Observations at higher frequencies were made in the search mode of the Parkes ultra-wideband low-frequency (UWL; Hobbs et al., 2020) receiver that spans the frequency range from 704 to 4032 MHz, and followed analysis procedures as described in Dai et al. (2019).

The best detection was made in the uGMRT Band 3 frequency range, where S/N$\sim$300 was achieved in one of the observing sessions in $\sim$30-min integration. Despite the severe RFI contamination of the Parkes data, the pulsar was clearly detected in the low band range 750-1300 MHz, as shown in Fig. 5. Estimated flux densities are $\sim$4.2 and 2 mJy, respectively at 400 and 650 MHz (from uGMRT imaging, see Fig. 3). The pulsar was also detected in the TIFR GMRT Sky Survey (Intema et al., 2017), with a flux density of $\sim$19 mJy (at 150 MHz) and also in the ASKAP-low and -high bands, with flux densities of $\sim$1.3 mJy (at 888 MHz) and $\sim$0.3 mJy (at 1.5 GHz), respectively (E. Lenc, private communication). The combination of these measurements suggest a spectral index $\alpha \sim -1.6$ for this pulsar, assuming no turnover down to $\sim$150 MHz. However, as reported in McSweeney et al. (2022), the pulsar exhibits a large nulling fraction of $\sim$75%, and complex sub-pulse drifting behaviour, including rapid changes of the drift rate and consistent evolution within its two main drift modes. Further analysis using these data are deferred to a future publication (Janagal et al. in prep.).

4. Pulsar discoveries and census

As described in § 2, a first-pass search processing is currently in progress, to realise a shallow survey for long-period pulsars. About $\sim$10% of the data collected so far have been processed in this mode, though it covers $\sim$55% of the planned sky coverage. Only a small fraction ($\lesssim$3%) of the candidates have been examined for promising candidates to follow up, resulting in four pulsar discoveries, one of which is an independent discovery of a GBNCC pulsar candidate, and another a re-discovery of a pulsar that was originally found in the Parkes 70cm survey (Manchester et al., 1996) but reported with an incorrect name and DM. The processing has also led to a re-detection of 120 previously known pulsars, which brings the number of MWA pulsar detections to 180, a significant improvement over the initial census (at 185 MHz) reported in Xue et al. (2017).

Table 4. Timing solution for PSR J0026–1955 using Tempo2.

Timing solution and best-fit metrics	
J2000 Right ascension (hh:mm:ss)	00:26:36.3(2)†
J2000 Declination (dd:mm:ss)	–19:55:59.3(30)†
Spin frequency, f (Hz)	0.765607774650(8)
First spin frequency time-derivative, $\dot{f}$ ($\times10^{-16}$ Hz s^{-1})	–2.58(9)
Dispersion measure, DM (pc cm^{-3})	20.81(1)
Reference epoch (MJD)	58724
Observing timespan (MJD)	58427-59020
Solar system ephemeris	DE430
Time ephemeris	FB90
Clock standard	TT(BIPM)
Units	TDB
Reduced-χ^2	1.32
Degrees of freedom	40
RMS timing residual (μs)	1332
Derived quantities	
Galactic longitude, l (°)	83.2963
Galactic latitude, b (°)	–80.8295
Spin period, P (s)	1.30615183533(1)
First spin period derivative, $\dot{P}$ ($\times10^{-16}$ s s^{-1})	4.4(1)
Characteristic age, τ_c (Myr)	47
Surface magnetic field strength, B_S ($\times10^{11}$ G)	7.7
Spin-down luminosity, $\dot{E}$ ($\times10^{31}$ erg s^{-1})	2.3

† The position of the pulsar was fixed at the uGMRT imaging position, as given in Section 3.1.

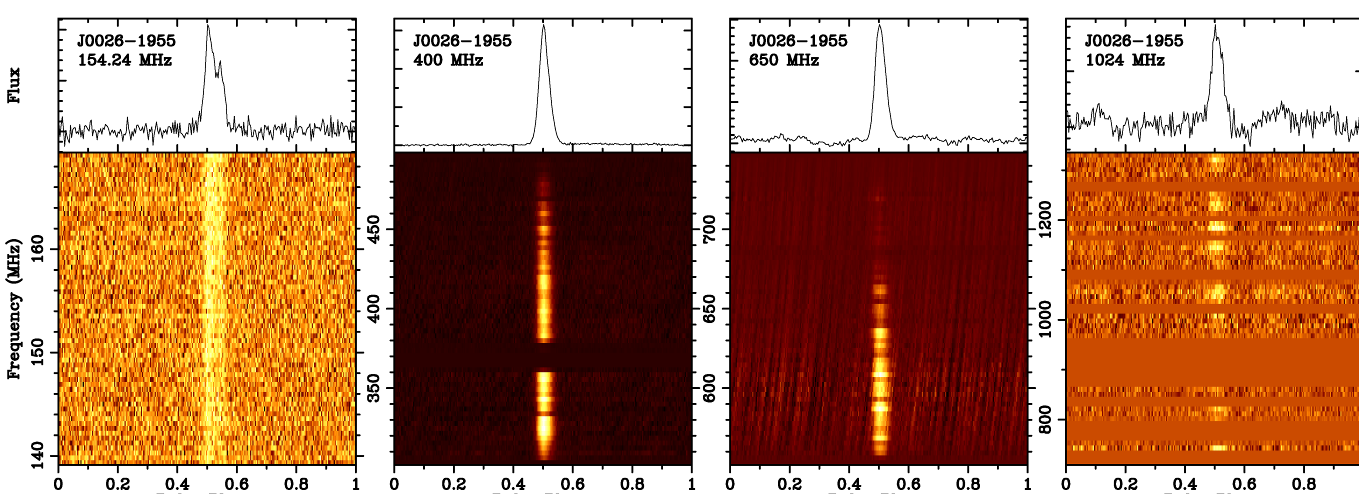


Figure 5. Detection plots of PSR J0026–1955 with the MWA (left panel), uGMRT (two central panels), and Parkes (right panel) telescopes, spanning a frequency range from 140 to 1400 MHz: the top panel is the integrated pulse profile and the waterfall plot below shows the pulse strength vs. pulse phase and frequency. MWA observations were made with the Phase 2 compact configuration of the array, whereas those with the uGMRT made use of the 200 MHz mode of the phased-array beamformer comprised of 11-13 antennas located within the central square. Parkes observations were made using the Ultra-Wideband Low-frequency receiver (700-4032 MHz); however, the pulsar was detected only in the band below 1.4 GHz. The profiles each have been downsampled to 256 bins across pulse phase and 64 frequency channels for plotting clarity.

All four pulsars are being followed up with Parkes and the uGMRT, and also using archival and new data from the MWA, for detailed characterisation including their timing, variability, and early science, and also with the intent to develop and demonstrate effective follow-up strategies. Basic parameters of these pulsars are summarised in Table 2, and we elaborate on some specifics in the sections below.

4.1 Individual pulsar details

4.1.1 PSR J0036–1033

PSR J0036–1033 is the first new pulsar discovery from the SMART survey, the details and initial follow-up of which have been reported in Swainston et al. (2021). This non-recycled pulsar with a period P = 0.9 s and a DM = 23.123 pc cm^{-3} has a fairly typical magnetic field strength ($B \sim 4.4 \times 10^{11}$ G) and characteristic age ($\tau_c \sim 67$ Myr) but has a spectral index $\alpha = -2.0 \pm 0.2$. An estimated luminosity at 1400 MHz, L_{1400} ~0.1 mJy kpc^2, places this pulsar in the lowermost two percentile of the currently known population of long-period pulsars in luminosity. Its DM and a location at a high Galactic latitude ($b \approx -72.9°$) make it an excellent target for scintillation and variability studies for probing the nature of plasma turbulence in a region where it is poorly constrained. The related observations are currently under way at the uGMRT and the Five-hundred-metre Aperture Spherical Telescope (FAST) and will be reported in a future publication.

4.1.2 PSR J0026–1955

The "discovery" of PSR J0026–1955 revealed some remarkable features of the SMART survey; most notably, the complexity of the tied-array beam pattern, resulting from a large fraction of the tiles configured as hexagonal layouts (see Paper I; Figs. 7 and 8). This can result in multiple detections of pulsars through the near and far side (grating) lobes, especially when the pulsar is sufficiently bright. For instance, PSR J0026–1955, which was initially detected as a 11σ candidate (in a 10-min observation) was eventually re-detected in a different pointing, almost ~45′ offset from the initial position, and with a much higher significance of S/N = 60, leading to the revelation that the initial detection was in fact through one of the grating lobes.

The pulsar was also particularly noted for its sub-pulse drifting nature which became the focus of immediate investigation. Incidentally, this turned out to be an independent discovery, as the pulsar was first reported as a candidate in the Green Bank Northern Celestial Cap (GBNCC) survey data; nevertheless, it was blindly discovered in our SMART processing. Further details of the pulsar, including analysis of its intriguing sub-pulse drifting and long-duration nulls, are reported in McSweeney et al. (2022).

4.1.3 PSR J1002–2036

The discovery of PSR J1002–2036 followed the new (revised) scheme for candidate selection and scrutiny, as described in Section 3.3 of Paper I. It is a long-period pulsar with P = 1.67 s and a moderate DM = 43.172 pc cm^{-3}. The NE2001 model of electron density (Cordes & Lazio, 2002) places it at a distance of ~1.4 kpc. Its non-detection in the Parkes 70 cm survey implies a spectral index $\alpha \lesssim -1.8$, and non-detections in the TGSS (TIFR GMRT Sky Survey) and NVSS (NRAO VLA Sky Survey) continuum imaging sky surveys, which reached rms sensitivity limits of ~5 mJy beam^{-1} and ~0.5 mJy beam^{-1} (in the pulsar vicinity) at their respective frequencies (i.e. 150 MHz and 1400 MHz), implying a flux density at 150 MHz, $S_{150} \lesssim$ 10 mJy. This hints at the possibility of the pulsar being another low-luminosity object, with an implied $L_{1400} \lesssim 0.3$ mJy kpc^2, which is confirmed by our recent Parkes detection, suggesting $S_{1400} \sim 0.1$ mJy, and hence akin to PSR J0036–1033. The pulsar is currently being followed up for timing and localisation (via imaging) using Parkes and the uGMRT.

4.1.4 PSR J1357–2530

Of the 120 redetections from SMART data processing (see § 4.2), PSR J1357–2530 warrants some additional contextual discussion. It was first "discovered" in the untargetted SMART search workflow as a 6σ candidate in a 10-minute observation, with a period (P) of 0.912 s and DM of 16.046 pc cm^{-3}(see Fig. 2). Follow-up processing of the full 80-min observation resulted in a significantly improved detection, with a four-fold increase in S/N, as shown in the figure. This pulsar has a small duty cycle of ~2-3%, and the DM implies a distance of ~0.8 kpc as per the NE2001 model of (Cordes & Lazio, 2002). However, a closer examination of the published literature including those from low-frequency surveys with Parkes and the Green Bank Telescope (GBT), has essentially confirmed that this is a rediscovery. The Parkes 70 cm survey appears to have been reported this as PSR J1358–2533 with a similar period but with a significantly discrepant DM = 28 ± 3 pc cm^{-3} and at ~20′ offset from our MWA position (Manchester et al., 1996). The DM was subsequently revised upward by D'Amico et al. (1998) to 31.3 ± 1 pc cm^{-3}. It appears that GBNCC has re-found the pulsar but with a DM = 16.0 ± 0.2 pc cm^{-3} (McEwen et al., 2020). Even so, the position (and hence the pulsar's exact name) remained uncertain and a timing solution is currently not available. The pulsar also appears to be another low-luminosity object, even if we are to assume a spectral index (α) of −1.6.

In order to resolve this ambiguity, we recently undertook uGMRT follow-up observations of this pulsar (GTAC Cycle 43), where we used an observing set-up that is similar to those described in § 3.1 (i.e. concurrent imaging and phased-array beams). Following an initial non-detection, which is attributable to a poorly localised position, imaging of the recorded visibility data revealed multiple (five) compact sources in the field within ~ 5′ from the phase centre; one of these turned out to be the pulsar, as shown in the lower panels of Fig. 3. This was confirmed in subsequent observations, where we cycled through the prospective sources by making separate phased-array beam observations. Table 5 gives a summary of the pulsar positions from our uGMRT imaging along with the initial MWA position (from the TAB localisation). The pulsar position, with R.A. 13h57m24s, and decl. −25°30′39″, while

Table 5. Localisation summary of PSR J1357–2530

Telescope/System	Method	Right Ascension (J2000)	Declination (J2000)
MWA VCS	Tied-array beams	$13^h57^m34^s$	$-25°33'11''$
uGMRT Band 3	Imaging	$13^h57^m24.40^s$	$-25°30'39.0''$
uGMRT Band 4	Imaging	$13^h57^m24.23^s$	$-25°30'38.7''$
Final position	Imaging	$13^h57^m24^s.3(2)$	$-25°30'38''.9(4)$

precisely determined down to $\lesssim 0.3''$, has a systematic offset of $\sim 3''$, possibly due to ionospheric refraction (cf. Swainston et al. 2022a). The estimated flux densities are $\sim$1 mJy and $\sim$0.5 mJy at 400 and 650 MHz, respectively. A summary of the pulsar parameters are included in Table 2. The new position warrants renaming the pulsar to PSR J1357–2530.

4.2 Redetections of known pulsars

As described earlier, a secondary goal of the SMART survey is to map out the southern sky for low-frequency detections of known pulsars. This is important for two main reasons. Firstly, all past large pulsar surveys in the southern hemisphere have been at frequencies $\gtrsim$400 MHz (e.g., Manchester et al., 1978, 1996, 2001; Keith et al., 2010). With the majority of the pulsars in the southern sky originally found and followed up at such high frequencies, low-frequency information ($\lesssim$300 MHz) is lacking for a substantial number of known pulsars, especially for those at declination, $\delta \lesssim -30°$. Despite the MWA opening a new low-frequency window for pulsar astronomy in the south, the limitations of legacy VCS (e.g., a maximum recording capacity of 1.5 hr) [a] and the logistics of handling large data rates prevented undertaking a complete pulsar census in an efficient manner. In an effort to partly address this, and as a preparatory work toward SKA-Low science, Xue et al. (2017) carried out the first pulsar census with the MWA at 185 MHz, using the then available resources and data sets (covering $\sim$55% of the sky) and software and processing capabilities (i.e., incoherent detection, reaching $\lesssim$10% of the full coherent beam sensitivity). This led to the low-frequency detections of 50 pulsars (including 6 millisecond pulsars), 10 of which were detected for the first time at low frequencies. This modest sample was also used for simulation studies and forecasting the detectable population of pulsars with SKA-Low, as summarised by Xue et al. (2017).

A summary of re-detections from the SMART processing thus far is shown in Fig. 6, where we have also shown those from non-SMART observations (i.e., archival data or other VCS-based projects). In total there have been 120 re-detections from the SMART project; integrated profiles of these (at 155 MHz) are shown in Fig. 8. Table 6 provides a summary of these detections, along with the pulsar parameters P and DM, and the signal-to-noise ratio of detection $(\mathrm{S/N})_{\rm det}$. Given the strong direction and elevation dependencies of the MWA's sensitivity, we have accounted for the expected degradation in $(\mathrm{S/N})_{\rm det}$ due to the pulsar's offset within the primary beam (relative to the beam centre), while estimating the mean flux density at the observing frequency (listed in the column 6 of Table 6). As a result of the large extent of the MWA's primary beam, these offsets can be as large as $\sim$10–20° relative to the centre of the beam; for example, PSR J0034–0721, a bright long-period pulsar (and a well-known sub-pulse drifter; McSweeney et al. 2017), which would be detected with S/N $\sim$ 400 in $\sim$1 hr observation, will likely be detected with $(\mathrm{S/N})_{\rm det} \lesssim 100$ when observations are made at an elevation of $\sim$30° and at $\sim$10° offset from the beam centre.

Including 57 pulsars from non-SMART observations, 18 of which are from targeted observations toward PSR J1822–2256 (from the G0071 project; by Janagal et al.), this brings the current tally to 180 pulsars detected by the MWA. This is more than triple the number of pulsar detections with the MWA since the publication of Xue et al. (2017), but with the important distinction that many of these are full coherent beam detections, and the data can be reprocessed for full polarimetric information and/or higher time resolution (down to $\lesssim$1 μs) depending on the scientific case (e.g., millisecond pulsars). Of the 177 pulsars shown in Fig. 6 (and summarised in Figs. 8 and 9, and Tables 6 and 7), the detection of 96 was facilitated by the SMART survey data, i.e. doubling of the number of pulsars detected with the MWA. For 34 pulsars, these are also the first low-frequency detections ($\lesssim$300 MHz); 30 of our pulsars have also been detected by the LOFAR (Bilous et al., 2016). Collectively, these will help extend the low-frequency coverage of pulsars, providing a useful sample for further detailed studies of pulsar emission and/or population analysis.

For many pulsars detected in SMART observations (Fig. 8), there have been multiple detections, by virtue of our sky tessellation strategy (Fig. 1), where the adjacent SMART pointings overlap $\sim$10° in R.A. and $\sim$12° in declination. In most such cases, we have selected the best detection. The number of phase bins $N_{\rm bin}$ is chosen to optimise $(\mathrm{S/N})_{\rm det}$ while retaining the ability to discern main profile features, and varies from 64 to 1024. For MSPs with short periods ($P \lesssim 5$ ms), $N_{\rm bin} \approx P_{\rm ms}/0.1$, where $P_{\rm ms}$ is the period in ms.

4.2.1 Detection sensitivity and flux densities

The re-detections from SMART are used to ascertain the survey sensitivity at 150 MHz by comparing the measured pulsar flux densities $S_{150}^{\rm meas}$ with their expected values $S_{150}^{\rm exp}$. To estimate $S_{150}^{\rm meas}$, folded profile data were flux density calibrated using the method outlined in Meyers et al. (2017). In brief, this makes use of the array factor formalism whereby the tied-

[a] The new high-time-resolution system (MWAX VCS) is capable of recording over much longer durations, up to $\sim$5-6 hours.

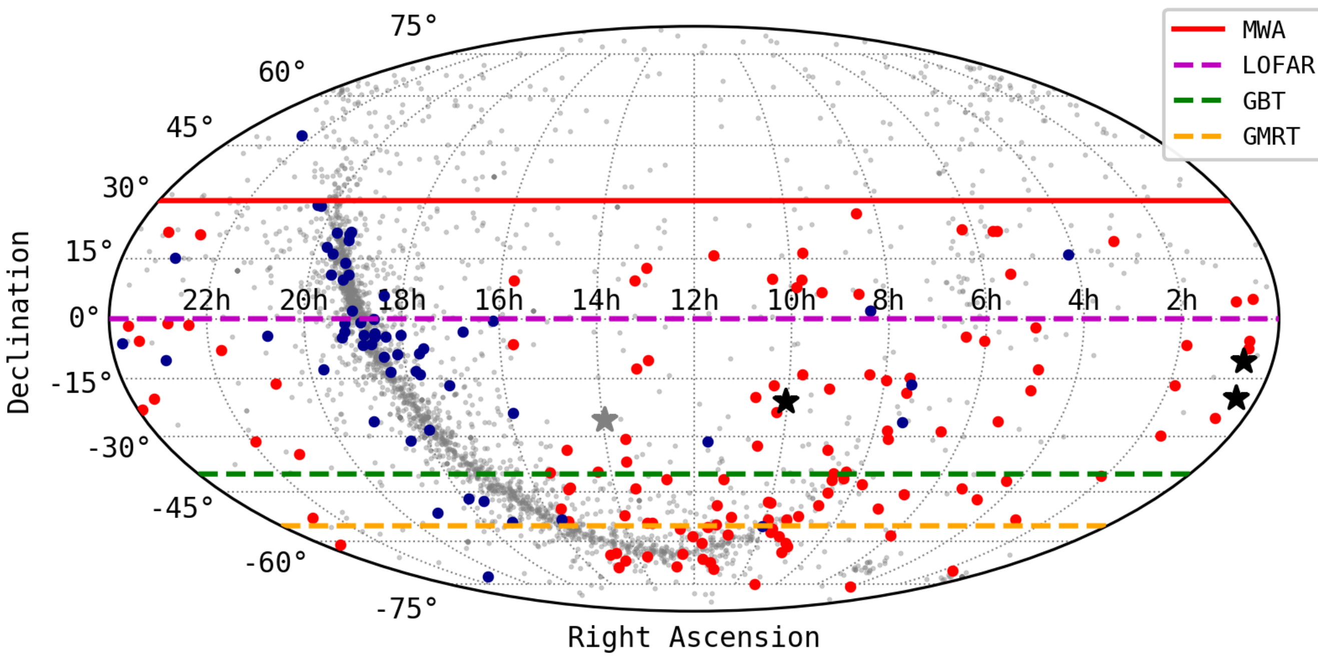


Figure 6. All-sky distribution of known pulsars in the ATNF pulsar catalogue (grey filled circles). The 120 pulsars detected in the SMART processing are shown as red filled circles, along with 57 pulsars detected from the processing of non-SMART MWA observations (shown as filled circles in dark blue, respectively, for incoherent and coherent beam detections). The black star symbols are the three new pulsar discoveries from the SMART, and the grey star is re-discovery of a previously incorrectly characterised pulsar. The declination limit of the SMART survey ($\delta < +30°$) is shown as the solid red line and for surveys with other (northern) telescopes, they are shown as dashed lines at the respective lower limits in declination (i.e., $\delta > 0°$ for LOTAAS, $\delta > -40°$ for GBNCC and $-40° > \delta > -55°$ for GHRSS).

array beam patterns are simulated by modelling them as the product of the tile beam pattern (primary beam response) and the array factor (in this case for the compact configuration of the Phase II array). This analysis yields estimates of the system temperature (T_{sys}) and gain (G), which are then used to estimate the system equivalent flux density, SEFD = T_{sys}/G. The simulations also naturally take into account the strong directional dependencies of these parameters. The variability in T_{sys} and G over the duration of observation is accounted for as a source of error in the flux density estimate.

The expected flux densities S_{150}^{exp} are essentially based on the extrapolation from the spectral forms deduced using the published flux density measurements of pulsars. This involved the use of a large body of flux density measurements made available by Jankowski et al. (2018) as well as a number of other past publications. The model fits to the spectra are based on the algorithms described in the work of Jankowski et al. that employs the Akaike information criterion (AIC) to determine the best spectral model. Further details on the database repository and software description are presented in Swainston et al. (2022b). The uncertainties in S_{150}^{exp} thus largely reflect the quality and uncertainty of the model fit to the spectra (e.g., the error on the spectral index, or other spectral characteristics). An important caveat is that the bulk of the flux density measurements are from observations at frequencies $\gtrsim$400 MHz and as a result may likely over-predict the expected values of S_{150}^{exp} for pulsars that exhibit turnover, or a spectral break, or flattening at low frequencies.

A comparison of the measured flux densities of detected pulsars and the expected values as described above is shown in Fig. 7. This includes 100 pulsars for which reasonable estimates of S_{150}^{exp} were possible (i.e., four or more measurements available to allow meaningful estimates of the spectral form and the index α), which limited the analysis to $\sim$80% of the detected pulsars.

As shown in the figure, within the caveats of the uncertainties associated with S_{150}^{meas} and S_{150}^{exp} (e.g., from beam simulations, and the spectral model fits) and the assumptions involved (e.g., spectral extrapolation to 150 MHz), we find there is reasonable agreement, with the measured flux densities within a factor of two of their expected values. Evidently there are a small number of outliers where the analysis tends to over-predict S_{150}^{exp}, and this may be to do with a spectral extrapolation error. In the case of some high DM pulsars, it is also possible there may be an underestimation of S_{150}^{meas}, especially in the cases where the scatter broadening is substantial. The ratio between the measured and expected values is $S_{150}^{meas}/S_{150}^{exp} = 1.05^{+0.42}_{-0.31}$ (after excluding a small number of outlier points where the ratio >10 or <0.1). Given this, and with the caveat that in general large flux density variabilities expected at low frequencies (as much as by a factor of $\sim$2–3 for moderate to high-DM pulsars, and even larger for low-DM ones), this provides a good demonstration that our SMART data processing is attaining a detection sensitivity in line with the expectations.

The measured flux densities of detected pulsars also validate

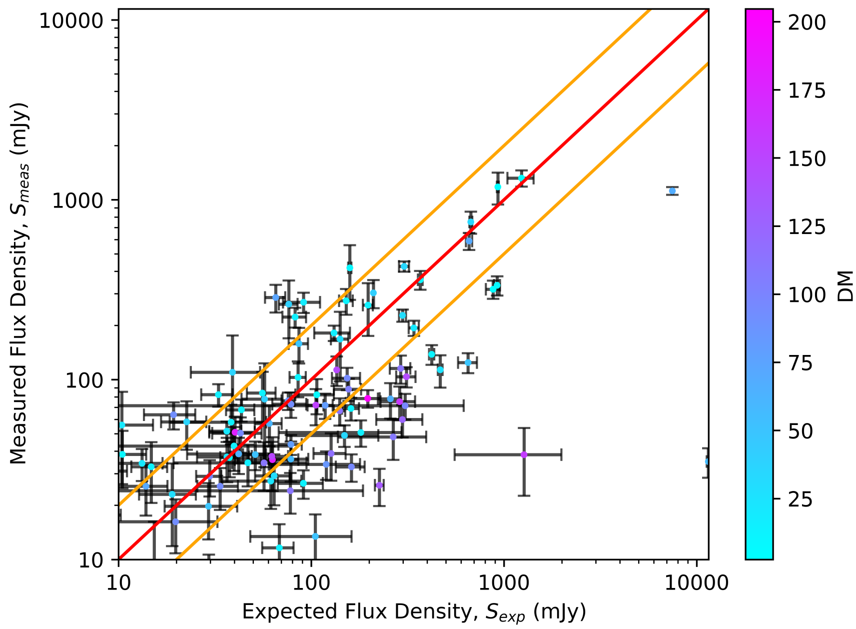


Figure 7. Measured flux densities $S_{\rm meas}$ against expected flux densities $S_{\rm exp}$ for 100 re-detections from the SMART survey processing; the measured values are corrected for the pulsar's offset relative to the centre of the primary beam, and can be as much as a factor of three. The expected values are extrapolations based on spectral fitting on the published flux density measurements of the pulsars (see text for details). The red line indicates where the two flux densities are equal whereas the grey-shaded region indicates a factor of two difference.

the minimum expected sensitivity ($S_{\rm min}$) for the shallow pass of our survey, where $S_{\rm min} \sim 10$ mJy for a 10σ detection of long-period pulsars (see Fig. 7). As seen from the figure, the faintest pulsar detections are $S_{150}^{\rm meas}$ ∼7–8 mJy. In general, the measurements of low to moderate-DM pulsars are in better agreement compared to high-DM ones (i.e., $\gtrsim$50 pc cm^{-3}). Further details on the data used for the analysis, and the software description, are available in Swainston et al. (2022b).

4.2.2 Data release

Considering the inherent difficulties in accessing and processing VCS recorded data for pulsar detections and searching, we will make beamformed data of re-detected pulsars publicly accessible via a dedicated database repository (to be served by Data Central). We will adopt the preferred data format by other large pulsar databases (e.g., Hobbs et al., 2011), i.e., folded archives in 10-s sub-integrations, with all 3072 channels and in full polarisation (i.e. four Stokes). For millisecond pulsars, we will provide coherently-dedispersed profiles in 1024 or more phase bins, in 24 coarse channels (1.28 MHz). Our intent is a continual growth of this database as further detections accrue from the ongoing and future data processing. Given the paucity of low-frequency pulsar detections in the southern sky, we hope this will become a useful resource, and potentially a reference catalogue of low-frequency pulsar detections in the SKA-Low era. Additionally, SMART survey raw data from 2018-2019 will be made available via a data retention project supported by Australian Research Data Commmons.[b]

[b]See https://doi.org/10.25917/qd25-pg50 for data access.

5. Summary and conclusions

The SMART survey, enabled by the advent of the Phase II upgrade of the MWA, is an ambitious all-sky project to search for pulsars and fast transients at low frequencies. It exploits the large FoV and voltage capture functionality of the MWA, the combination of which brings a survey efficiency of ∼450 deg^2 hr^{-1} , but at the expense of large data rates of 28 TB hr^{-1}, and consequently, substantial computational costs in beamforming and search processing. The execution of the survey relies on the availability of the compact configuration of the Phase II array. Through a series of four dedicated campaigns over the past few years, the data collection part of the survey is now ∼75% completed.

In the first-pass processing as described in Paper I, where 10 min of data from each observation (out of 80 min) are processed (in 2358 trial DMs, out to a maximum DM of 250 pc cm^{-3}), effectively a shallow survey is performed, reaching a sensitivity about one-third of that will eventually be attainable with the planned deep-pass processing. Already three new pulsars have been found from the initial processing, where ∼3% of the candidates have been scrutinised for promising ones. This initial processing has also led to re-detection of 120 previously known pulsars, thus bringing the total tally of MWA-detected pulsars to 180, i.e. more than a tripling of the number of pulsars detected with the MWA before the advent of the SMART survey.

The voltage recording strategy employed for the survey enables a multitude of avenues for follow-ups and confirmations, including improved detection and localisation to sub-arcminute position, thereby facilitating prompt follow-ups

using sensitive telescopes such as Parkes and uGMRT that operate at $\gtrsim$300 MHz. Not only that this strategy is enabling an accelerated convergence to initial pulsar timing solution; e.g., by taking advantage of high-resolution ($\sim$arcsecond) imaging with the uGMRT, archival VCS observations (where available) can also be potentially exploited to obtain a full coherent timing solution, as demonstrated in this paper.

The early discoveries and science from the SMART provide an excellent demonstration of the potential benefits of using a next-generation survey instrument such as the MWA, in tandem with current-generation instruments (e.g., Parkes, uGMRT) for fruitful scientific exploitation. For example, PSR J0036–1033, the first MWA-discovered pulsar turned out to be a low-luminosity object (Swainston et al., 2021), and a promising target for probing the high-b turbulent plasma. PSR J0026–1955, the second pulsar discovered, exhibits intriguing sub-pulse drifting patterns and has a large nulling fraction of $\sim$77% (McSweeney et al., 2022). Follow-up studies of these pulsars are in progress with the uGMRT and FAST. The third pulsar, PSR J1002–2036, another potential low-luminosity object, is currently being followed up using the uGMRT and Parkes, as well as with the MWA. Finally, for PSR J1357–2530, a pulsar originally reported in the literature with an incorrect name and DM, we have obtained a precise position via uGMRT follow-up to facilitate a high-resolution imaging and source identification.

The initial discoveries and results presented in this paper hint at a promising future for the SMART. As efforts around data processing and candidate scrutiny ramp up over the coming years, we anticipate the discovery rate to increase. The SMART is well positioned to emerge as a low-frequency version of the HTRU survey with Parkes, and as an important reference for even more ambitious surveys planned with the SKA-Low.

Acknowledgement

We thank an anonymous referee for several useful comments that helped to improve the content and presentation of this paper. The scientific work made use of Inyarrimanha Ilgari Bundara, the CSIRO Murchison Radio-astronomy Observatory. We acknowledge the Wajarri Yamaji people as the traditional owners of the Observatory site. This work was supported by resources provided by the Pawsey Supercomputing Centre with funding from the Australian Government and the Government of Western Australia. This work was supported by resources awarded under Astronomy Australia Ltd's ASTAC merit allocation scheme on the OzSTAR national facility at the Swinburne University of Technology. The OzSTAR program receives funding in part from the Astronomy National Collaborative Research Infrastructure Strategy (NCRIS) allocation provided by the Australian Government. The GMRT is run by the National Centre for Radio Astrophysics of the Tata Institute of Fundamental Research, India. The Parkes radio telescope is part of the Australia Telescope National Facility which is funded by the Australian Government for operation as a National Facility managed by CSIRO.

Software: We acknowledge the use of the following software/packages for this work: CASA (McMullin et al., 2007), DSPSR (van Straten & Bailes, 2010, 2011), PRESTO (Ransom, 2001, 2011), PSRCHIVE (Hotan et al., 2004; van Straten et al., 2011), Tempo2 (Hobbs et al., 2006; Hobbs & Edwards, 2012), PINT (Luo et al., 2019, 2021), PsrPopPy (Bates et al., 2014), Nextflow (Di Tommaso et al., 2017).

References

Archibald, A. M., Stairs, I. H., Ransom, S. M., et al. 2009, Science, 324, 1411
Bailes, M., Jameson, A., Abbate, F., et al. 2020, PASA, 37, e028
Balakrishnan, V., Champion, D., Barr, E., et al. 2021, MNRAS, 505, 1180
Bates, S. D., Lorimer, D. R., Rane, A., & Swiggum, J. 2014, MNRAS, 439, 2893
Bell, M. E., Murphy, T., Johnston, S., et al. 2016, MNRAS, 461, 908
Bhattacharyya, B., Cooper, S., Malenta, M., et al. 2016, ApJ, 817, 130
Bilous, A. V., Kondratiev, V. I., Kramer, M., et al. 2016, A&A, 591, A134
Cordes, J. M., & Lazio, T. J. W. 2002, arXiv e-prints, astro
Dai, S., Lower, M. E., Bailes, M., et al. 2019, ApJ, 874, L14
D'Amico, N., Stappers, B. W., Bailes, M., et al. 1998, MNRAS, 297, 28
Di Tommaso, P., Chatzou, M., Floden, E., et al. 2017, Nature Biotechnology, 35, 316–319
Edwards, R. T., Hobbs, G. B., & Manchester, R. N. 2006, MNRAS, 372, 1549
Frail, D. A., Jagannathan, P., Mooley, K. P., & Intema, H. T. 2016, ApJ, 829, 119
Gupta, Y., Ajithkumar, B., Kale, H. S., et al. 2017, Current Science, 113, 707
Han, J. L., Wang, C., Wang, P. F., et al. 2021, Research in Astronomy and Astrophysics, 21, 107
Hobbs, G., & Edwards, R. 2012, Tempo2: Pulsar Timing Package, Astrophysics Source Code Library, record ascl:1210.015, ascl:1210.015
Hobbs, G., Miller, D., Manchester, R. N., et al. 2011, PASA, 28, 202
Hobbs, G., Manchester, R. N., Dunning, A., et al. 2020, PASA, 37, e012
Hobbs, G. B., Edwards, R. T., & Manchester, R. N. 2006, MNRAS, 369, 655
Hotan, A. W., van Straten, W., & Manchester, R. N. 2004, PASA, 21, 302
Intema, H. T., Jagannathan, P., Mooley, K. P., & Frail, D. A. 2017, A&A, 598, A78
Izvekova, V. A., Kuzmin, A. D., Malofeev, V. M., & Shitov, I. P. 1981, Ap&SS, 78, 45
Jankowski, F., van Straten, W., Keane, E. F., et al. 2018, MNRAS, 473, 4436
Janssen, G., Hobbs, G., McLaughlin, M., et al. 2015, in Advancing Astrophysics with the Square Kilometre Array (AASKA14), 37
Kaur, D., Bhat, N. D. R., Tremblay, S. E., et al. 2019, ApJ, 882, 133
Keane, E., Bhattacharyya, B., Kramer, M., et al. 2015, in Advancing Astrophysics with the Square Kilometre Array (AASKA14), 40
Keith, M. J., Jameson, A., van Straten, W., et al. 2010, MNRAS, 409, 619
Kondratiev, V. I., Verbiest, J. P. W., Hessels, J. W. T., et al. 2016, A&A, 585, A128
Kramer, M., Stairs, I. H., Manchester, R. N., et al. 2021, Physical Review X, 11, 041050
Kuzmin, A. D., & Losovsky, B. Y. 2001, A&A, 368, 230
Luo, J., Ransom, S., Demorest, P., et al. 2019, PINT: High-precision pulsar timing analysis package, Astrophysics Source Code Library, record ascl:1902.007, ascl:1902.007
—. 2021, ApJ, 911, 45
Lyne, A. G., Burgay, M., Kramer, M., et al. 2004, Science, 303, 1153
Malofeev, V. M., Malov, O. I., & Shchegoleva, N. V. 2000, Astronomy Reports, 44, 436
Manchester, R. N., Lyne, A. G., Taylor, J. H., et al. 1978, MNRAS, 185, 409
Manchester, R. N., Lyne, A. G., D'Amico, N., et al. 1996, MNRAS, 279, 1235
Manchester, R. N., Lyne, A. G., Camilo, F., et al. 2001, MNRAS, 328, 17
McConnell, D., Hale, C. L., Lenc, E., et al. 2020, PASA, 37, e048

McEwen, A. E., Spiewak, R., Swiggum, J. K., et al. 2020, ApJ, 892, 76
McMullin, J. P., Waters, B., Schiebel, D., Young, W., & Golap, K. 2007, in Astronomical Society of the Pacific Conference Series, Vol. 376, Astronomical Data Analysis Software and Systems XVI, ed. R. A. Shaw, F. Hill, & D. J. Bell, 127
McSweeney, S. J., Bhat, N. D. R., Tremblay, S. E., Deshpand e, A. A., & Ord, S. M. 2017, ApJ, 836, 224
McSweeney, S. J., Bhat, N. D. R., Swainston, N. A., et al. 2022, ApJ, arXiv:2206.00805
Meyers, B. W., Tremblay, S. E., Bhat, N. D. R., et al. 2017, ApJ, 851, 20
Murphy, T., Kaplan, D. L., Bell, M. E., et al. 2017, PASA, 34, e020
Ransom, S. 2011, PRESTO: PulsaR Exploration and Search TOolkit, Astrophysics Source Code Library, record ascl:1107.017, ascl:1107.017
Ransom, S. M. 2001, PhD thesis, Harvard University
Ridolfi, A., Freire, P. C. C., Gautam, T., et al. 2022, A&A, 664, A27
Sanidas, S., Cooper, S., Bassa, C. G., et al. 2019, A&A, 626, A104
Shao, L., Stairs, I., Antoniadis, J., et al. 2015, in Advancing Astrophysics with the Square Kilometre Array (AASKA14), 42
Sieber, W. 1973, A&A, 28, 237
Stovall, K., Ray, P. S., Blythe, J., et al. 2015, ApJ, 808, 156
Swainston, N. A., Bhat, N. D. R., Morrison, I. S., et al. 2022a, PASA, 39, e020
Swainston, N. A., Lee, C. P., McSweeney, S. J., & Bhat, N. D. R. 2022b, PASA, 39, e056
Swainston, N. A., Bhat, N. D. R., Sokolowski, M., et al. 2021, ApJ, 911, L26
Tingay, S. J., Goeke, R., Bowman, J. D., et al. 2013, PASA, 30, e007
Tyul'bashev, S. A., Tyul'bashev, V. S., Oreshko, V. V., & Logvinenko, S. V. 2016, Astronomy Reports, 60, 220
van Haarlem, M. P., Wise, M. W., Gunst, A. W., et al. 2013, A&A, 556, A2
van Straten, W., & Bailes, M. 2010, DSPSR: Digital Signal Processing Software for Pulsar Astronomy, Astrophysics Source Code Library, record ascl:1010.006, ascl:1010.006
—. 2011, PASA, 28, 1
van Straten, W., Demorest, P., Khoo, J., et al. 2011, PSRCHIVE: Development Library for the Analysis of Pulsar Astronomical Data, Astrophysics Source Code Library, record ascl:1105.014, ascl:1105.014
Wayth, R. B., Tingay, S. J., Trott, C. M., et al. 2018, PASA, 35, 33
Xue, M., Bhat, N. D. R., Tremblay, S. E., et al. 2017, PASA, 34, e070
Zakharenko, V. V., Vasylieva, I. Y., Konovalenko, A. A., et al. 2013, MNRAS, 431, 3624

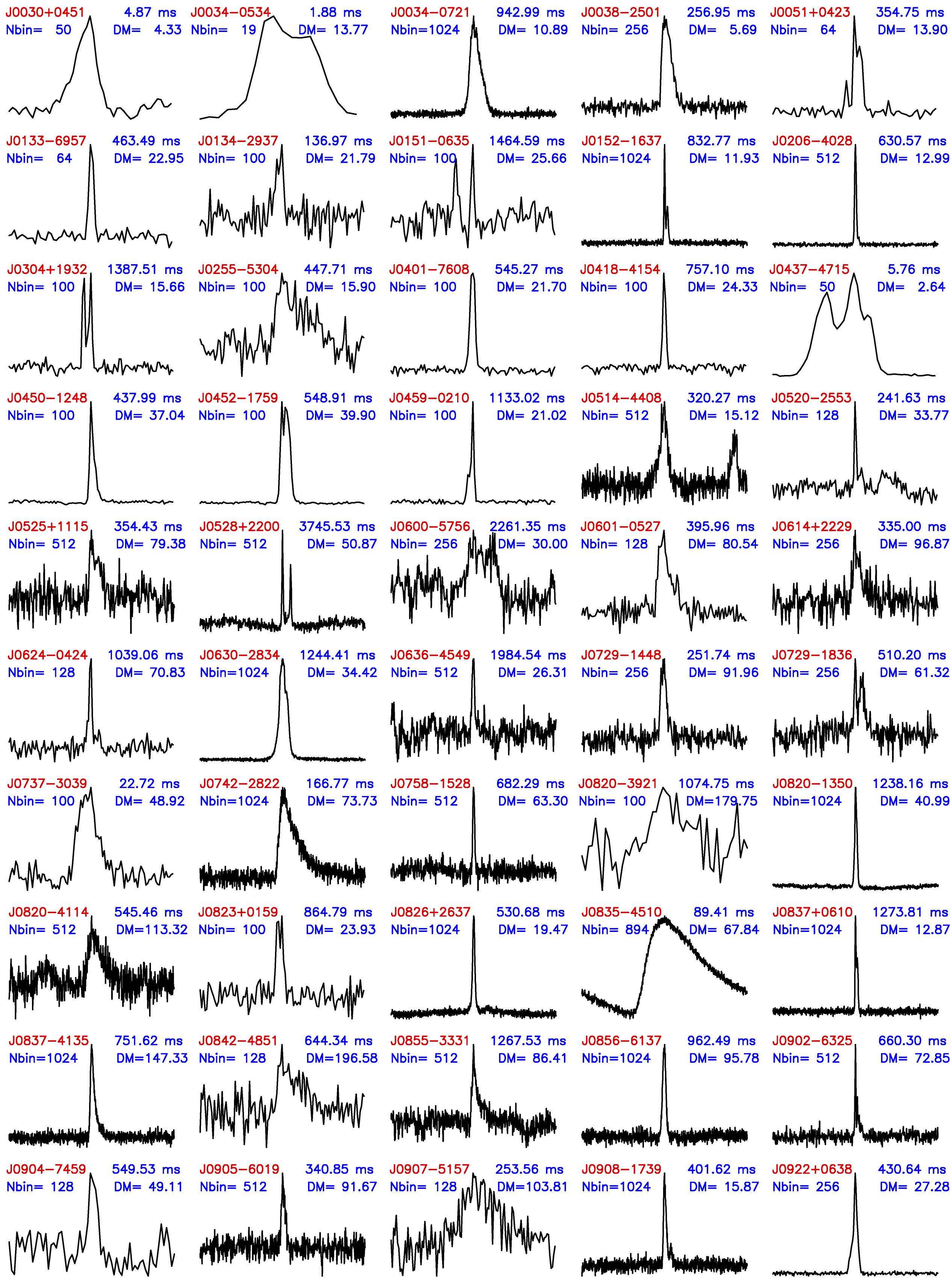


Figure 8. Integrated pulse profiles for 123 re-detected pulsars in the SMART data processing. The period, DM, and the number of phase bins are shown in each panel. All detections were made in the SMART survey band 140-170 MHz.

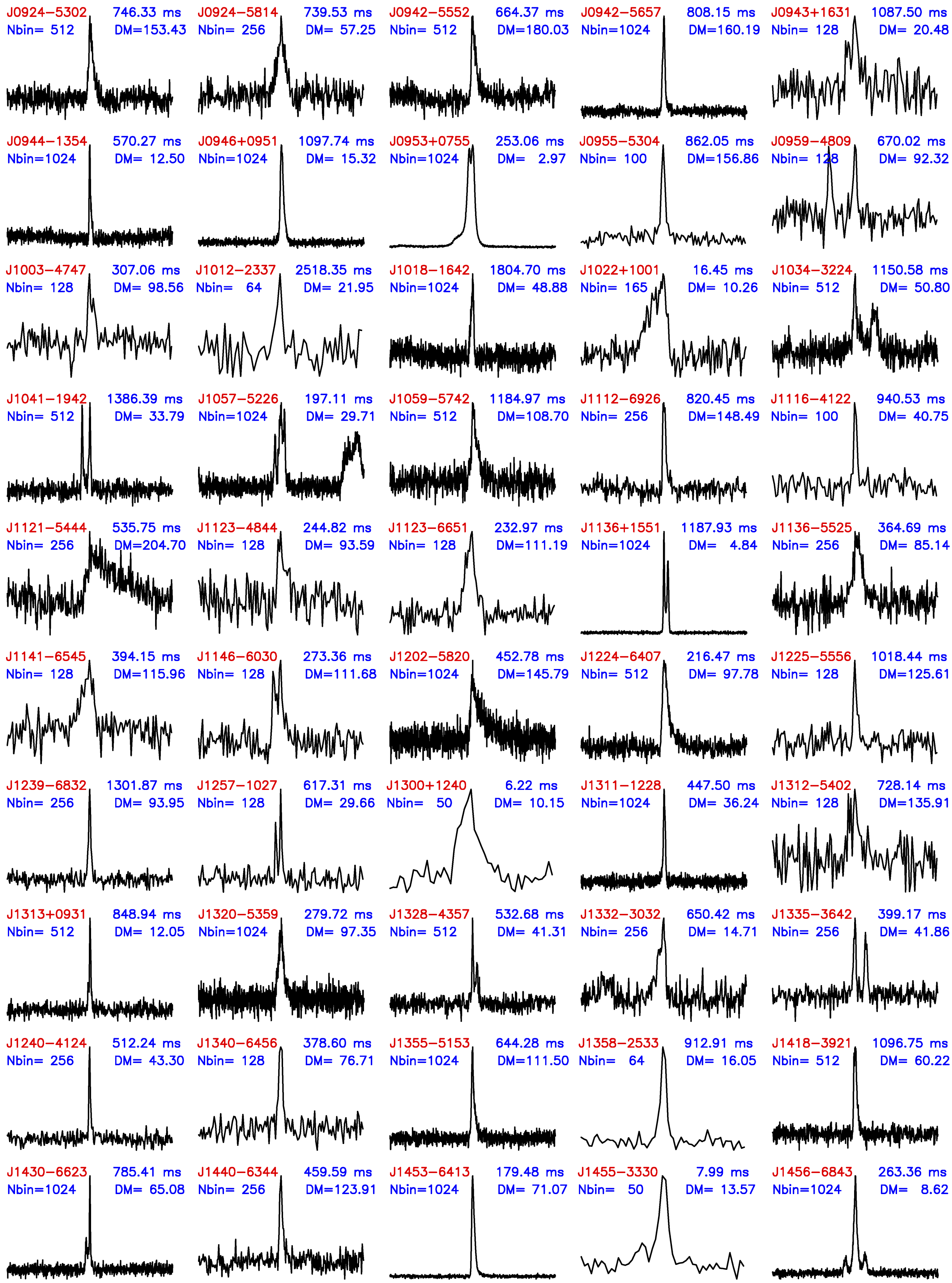


Figure 8. continued.

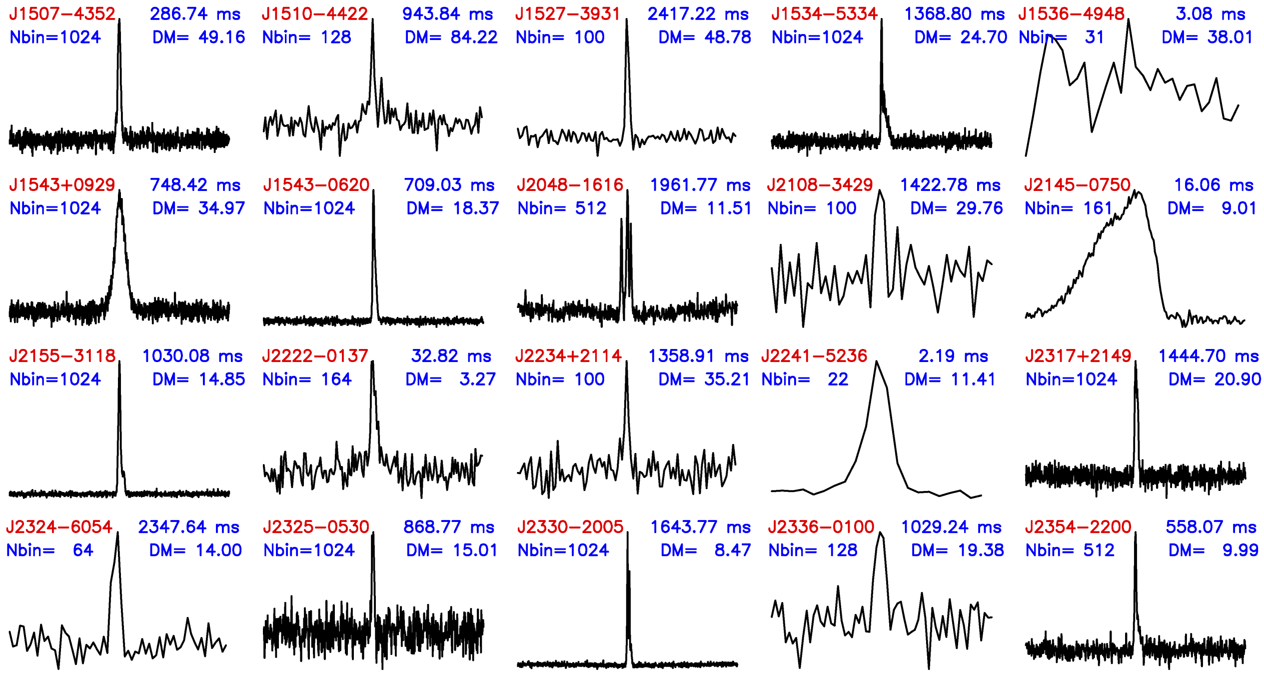


Figure 8. continued.

Table 6. Known pulsars detected in SMART survey observations.

Pulsar	Period (ms)	DM (pc cm^{-3})	Offset[1] (deg)	S/N	Mean flux density (mJy)	Obs ID	Notes[2]
J0030+0451	4.865	4.33	4.3	6.3	37±8	1255444104	G, L, g, P
J0034-0534	1.877	13.77	7.3	3.6	260±85	1255444104	M, G, L, g, P
J0034-0721	942.951	10.92	9.0	64.0	692±42	1255444104	P, E, W, U, M, L
J0038-2501	256.926	5.71	8.5	24.6	44±6	1226062160	g
J0051+0423	354.732	13.93	14.6	26.4	59±17	1225118240	U, L, g
J0133-6957	463.474	22.95	7.7	25.1	12±4	1227009976	
J0134-2937	136.962	21.81	20.7	10.6	11±3	1226062160	
J0151-0635	1464.665	25.66	17.3	13.9	8±3	1252177744	P, U, G
J0152-1637	832.742	11.93	11.5	74.4	131±17	1225462936	W, P, G, L
J0206-4028	630.551	12.9	11.1	68.2	1289±16	1224859816	M
J0255-5304	447.708	15.9	4.4	9.7	67±10	1253471952	
J0304+1932	1387.584	15.66	12.7	22.3	35±9	1254594264	P, W, L
J0401-7608	545.254	21.7	4.9	52.0	74±18	1255803168	
J0418-4154	757.119	24.33	3.9	42.3	38±11	1253991112	M, G
J0437-4715	5.757	2.64	15.4	6.2	1179±238	1257617424	M
J0450-1248	438.014	37.04	14.8	81.3	131±33	1256407632	P
J0452-1759	548.939	39.9	9.1	37.0	186±14	1257010784	P, M
J0459-0210	1133.076	21.02	3.9	81.5	68±22	1256407632	L, g
J0514-4408	320.271	15.12	13.3	13.2	91±8	1257617424	G
J0520-2553	241.642	33.77	3.8	20.5	18±5	1257010784	g
J0525+1115	354.438	79.42	12.8	8.7	44±6	1259685792	P, L
J0528+2200	3745.539	50.87	10.0	31.6	38±7	1259685792	L, P, E, W, P
J0600-5756	2261.365	30.0	2.9	8.6	27±3	1257617424	
J0601-0527	395.969	80.54	7.7	19.7	72±12	1259427304	P
J0614+2229	334.96	96.91	4.0	9.7	33±6	1259685792	P, L
J0624-0424	1039.076	70.84	16.3	13.4	26±8	1260638120	P, L
J0630-2834	1244.419	34.43	12.2	126.3	1353±91	1261241272	E, W, P, M, L
J0636-4549	1984.597	26.31	7.3	7.1	19±6	1258221008	
J0729-1448	251.659	91.89	12.6	12.9	64±11	1266155952	g
J0729-1836	510.16	61.29	13.6	12.4	72±11	1266155952	
J0737-3039A	22.699	48.92	4.9	22.2	173±28	1261241272	M, L, g
J0742-2822	166.762	73.73	23.0	11.1	362±40	1265470568	P, M
J0758-1528	682.265	63.33	6.0	21.2	39±9	1266155952	
J0820-1350	1238.13	40.94	0.9	112.7	411±48	1266155952	P
J0820-3921	1073.567	179.4	1.0	5.8	51±11	1265983624	W, P, M, L
J0820-4114	545.446	113.4	20.0	7.3	34±7	1265470568	g
J0823+0159	864.873	23.73	14.9	11.1	37±10	1266155952	M
J0826+2637	530.661	19.48	8.1	51.0	194±19	1265725128	L, P, E, W, U, M
J0835-4510	89.328	67.77	21.8	23.0	1121±55	1266680784	E, M
J0837+0610	1273.768	12.86	13.2	61.2	138±17	1265725128	L, P, E, W, P, M, U
J0837-4135	751.625	147.2	13.4	24.4	144±12	1266329600	M
J0842-4851	644.354	196.85	6.1	6.4	43±8	1266329600	
J0855-3331	1267.536	86.64	9.6	15.7	76±9	1265470568	M
J0856-6137	962.511	95.0	10.4	32.9	93±9	1266932744	M
J0902-6325	660.313	72.72	8.7	22.7	23±5	1266932744	
J0904-7459	549.554	51.1	3.4	6.9	13±4	1266932744	
J0905-6019	340.854	91.4	11.8	14.8	32±5	1266932744	
J0907-5157	253.558	103.72	4.7	7.1	89±13	1266329600	M, G
J0908-1739	401.626	15.88	20.6	20.2	62±6	1267283936	P, W, L
J0922+0638	430.627	27.3	5.0	45.0	184±17	1264867416	L, P, M, U
J0924-5302	746.338	152.9	17.1	14.1	64±9	1266680784	M, G
J0924-5814	739.505	57.4	14.4	10.2	30±5	1266932744	
J0942-5552	664.389	180.16	17.2	14.4	37±5	1266932744	M
J0942-5657	808.164	159.74	16.2	44.4	95±11	1266932744	M
J0943+1631	1087.418	20.34	11.7	11.1	34±7	1267111608	P, U, L
J0944-1354	570.264	12.5	11.6	24.8	27±5	1267283936	P
J0946+0951	1097.706	15.32	14.2	53.4	182±18	1267111608	L, P, E, U
J0953+0755	253.065	2.97	14.3	96.9	775±51	1267111608	L, P, E, U, M
J0955-5304	862.122	156.9	14.2	35.3	49±13	1266680784	
J0959-4809	670.086	92.7	9.8	19.0	110±8	1266680784	M
J1003-4747	307.074	98.49	9.1	17.6	29±7	1266680784	G
J1012-2337	2517.945	22.51	19.4	14.3	39±5	1268321832	M
J1018-1642	1804.695	48.82	20.8	13.1	16±5	1268321832	P
J1022+1001	16.453	10.25	16.4	10.7	68±10	1264867416	M, L, P
J1034-3224	1150.59	50.75	14.9	12.9	73±7	1268321832	g
J1041-1942	1386.368	33.78	14.6	24.5	49±7	1268321832	
J1057-5226	197.115	29.69	4.5	19.1	287±15	1267459328	M

Continued on next page

Pulsar	Period (ms)	DM ($pc\,cm^{-3}$)	Offset[1] (deg)	S/N	Mean flux density (mJy)	Obs ID	Notes[2]
J1059-5742	1185.003	108.7	17.5	21.6	49±10	1301240224	
J1112-6926	820.488	148.4	7.5	21.5	38±8	1301240224	M
J1116-4122	943.158	40.53	13.6	16.7	54±8	1267459328	M
J1121-5444	535.787	204.7	0.3	10.1	79±9	1267459328	M
J1123-4844	244.838	92.92	6.2	6.2	16±5	1267459328	
J1123-6651	232.976	111.2	8.3	11.3	40±8	1301240224	
J1136+1551	1187.913	4.84	14.1	151.6	318±37	1268063336	L, P, E, W, U, M
J1136-5525	364.713	85.11	1.9	7.4	34±6	1267459328	
J1141-6545	393.899	116.08	8.1	14.1	55±10	1301240224	M
J1146-6030	273.375	111.68	6.4	9.4	24±6	1267459328	
J1202-5820	452.803	145.41	14.1	13.9	88±11	1301240224	
J1224-6407	216.48	97.69	7.9	18.1	89±9	1301240224	
J1225-5556	1018.453	125.84	8.9	12	15±5.6	1267459328	
J1239-6832	1301.923	94.3	3.4	20.8	26±7	1301240224	
J1240-4124	512.242	44.1	1.1	22.2	34±9	1301412552	G
J1257-1027	617.308	29.63	5.0	18.0	29±9	1300809400	P
J1300+1240	6.219	10.17	15.6	9.4	34±9	1301847296	P, L, g
J1311-1228	447.518	36.21	16.4	26.1	51±9	1301847296	P
J1312-5402	728.154	133.0	15.8	8.5	26±6	1267459328	
J1313+0931	848.933	12.04	11.1	23.3	37±8	1301847296	L
J1320-5359	279.738	97.1	15.4	10.7	36±9	1301412552	G
J1328-4357	532.699	42.0	9.7	20.6	55±9	1301412552	
J1332-3032	650.434	15.1	4.7	12.1	51±9	1301674968	g
J1335-3642	399.192	41.82	11.6	13.2	49±9	1301412552	g
J1340-6456	378.622	76.99	8.9	12.1	24±7	1301240224	
J1355-5153	644.305	112.1	3.0	28.7	146±16	1302106648	
J1358-2533	912.971	16.05	3.3	26.0	27±8	1301674968	g
J1418-3921	1096.806	60.49	15.9	17.3	53±12	1302106648	g
J1430-6623	785.443	65.1	12.1	34.7	112±15	1302106648	M
J1440-6344	459.607	124.2	10.3	17.7	60±12	1302106648	M
J1453-6413	179.487	71.25	11.5	110.0	590±64	1302106648	M
J1455-3330	7.987	13.57	6.9	7.8	58±14	1302282040	
J1456-6843	263.377	8.61	15.3	51.1	433±36	1302106648	M
J1507-4352	286.758	48.7	4.8	25.1	125±16	1302282040	M
J1510-4422	943.871	84.0	5.5	13.2	51±13	1302282040	
J1527-3931	2417.605	48.8	7.3	24.0	31±13	1302282040	g
J1534-5334	1368.882	24.82	15.2	30.5	95±17	1302282040	M
J1536-4948	3.08	38.0	12.5	8.7	13±12	1302282040	
J1543+0929	748.448	34.98	15.8	26.5	426±28	1302540536	L, P, E, W, M
J1543-0620	709.064	18.3	14.6	69.0	270±35	1302712864	P, W, U, M, L, g
J2048-1616	1961.572	11.46	17.6	32.1	69±10	1222435400	P, M
J2108-3429	1423.102	30.22	11.7	7.5	13±5	1222435400	g
J2145-0750	16.052	9.0	17.7	9.2	61±11	1222697776	P, M, L
J2155-3118	1030.002	14.85	4.7	109.9	223±28	1222435400	M
J2222-0137	32.818	3.27	8.6	13.3	31±7	1221832280	L, g
J2234+2114	1358.745	35.08	5.5	5.2	9±7	1223042480	P, L, g
J2241-5236	2.187	11.41	12.0	27.9	705±37	1224252736	M
J2317+2149	1444.653	20.87	6.2	24.0	52±7	1223042480	L, P, U
J2324-6054	2347.488	14.0	11.8	17.0	12±4	1227009976	
J2325-0530	868.735	14.97	10.7	10.7	15±4	1222697776	g
J2330-2005	1643.622	8.46	9.7	112.4	87±14	1226062160	W, P, L
J2336-01	1029.8	19.6	15.3	11.7	53±10	1222697776	
J2354-22	557.996	9.9	4.2	25.2	16±3	1226062160	g

1 Target offset from observation centre.

2 Low-frequency (< 400 MHz) information available in the literature: 'M' for MWA-incoh/MWA-image (Bell et al., 2016; Murphy et al., 2017; Xue et al., 2017; Kaur et al., 2019), 'L' for LOFAR (Kondratiev et al., 2016; ?; Sanidas et al., 2019; ?), 'W' for LWA (Stovall et al., 2015), 'G' for GMRT (Bhattacharyya et al., 2016; Frail et al., 2016), 'g' for GBT-GBNCC (McEwen et al., 2020), 'E' for Effelsberg (Sieber, 1973), 'P' for Pushchino (Izvekova et al., 1981; Malofeev et al., 2000; Kuzmin & Losovsky, 2001; Tyul'bashev et al., 2016), 'U' for Ukrainian T-shaped Radio telescope-UTR2 (Zakharenko et al., 2013).

Table 7. Known pulsars detected with MWA observations not associated with SMART.

Pulsar	Period (ms)	DM (pc cm^{-3})	Offset[1] (deg)	Obs. freq. (MHz)	S/N	Beamform[2] type	Mean flux density (mJy)
J0407+1607	25.702	35.65	3.4	155	20.1	C	60±9
J0534+2200	33.392	56.77	0.1	155	538	C	6450±1200
J0725-1635	424.311	98.98	17.4	155	16.3	C	10±4
J0726-2612	3442.308	69.40	13.1	155	26.9	C	10±4
J0823+0159	864.873	23.73	8	185	9.6	I	35±5
J1001-5507	1436.631	130.32	1.4	185	6.8	I	53±5
J1141-3107	538.432	30.77	2.7	185	10.8	I	53±6
J1544-5308	178.554	35.16	7.6	185	8.8	I	102±15
J1555-2341	532.578	51.90	21.8	185	29.5	C	70±17
J1607-0032	421.816	10.68	11.9	185	6.7	I	270±59
J1645-0317	387.690	35.76	11.1	185	40.4	I	2224±107
J1709-1640	653.054	24.89	3.9	185	21.8	I	271±18
J1711-5350	899.233	106.10	1.9	185	6.1	I	20±15
J1731-4744	829.829	123.06	5.6	185	35.3	I	424±8
J1735-0724	419.335	73.51	11.9	185	5.6	C	25±11
J1741-0840	2043.082	74.90	10.6	185	7.0	C	19±9
J1743-1351	405.337	116.30	12.6	185	7.2	C	34±12
J1748-1300	394.133	99.36	11.1	185	9.4	C	34±11
J1751-4657	742.354	20.40	9.1	185	36.8	I	411±10
J1752-2806	562.558	50.37	2	185	143.1	I	2441±107
J1801-0357	921.493	120.37	5.5	185	6.4	C	12±6
J1807-0847	163.727	112.38	4.8	185	8.1	C	25±7
J1819-1318	1515.696	35.10	7.7	185	10.3	C	13±6
J1820-0427	598.082	84.44	1.9	185	197.7	C	946±166
J1823+0550	752.907	66.78	11.5	185	13.9	C	42±16
J1823-3106	284.054	50.24	4.6	185	10.8	I	105±15
J1825-0935	769.021	19.38	19.2	185	13.7	I	612±40
J1833-0338	686.733	234.54	3.5	185	5.1	C	86±12
J1834-0010	520.954	88.65	6.3	185	8.5	C	37±9
J1834-0426	290.108	79.31	3.3	185	51.2	C	341±61
J1839-0627	484.914	92.49	4.3	185	10.1	C	30±8
J1847-0402	597.809	141.98	6.5	185	8.6	C	67±11
J1849-0636	1451.319	148.17	6.7	185	8.7	C	66±12
J1851-0053	1409.065	24.00	8.6	185	11.4	C	18±7
J1900-2600	612.209	37.99	6.9	185	84.4	I	393±11
J1901+0156	288.219	105.39	12.4	185	11.3	C	40±10
J1902-5105	1.742	36.25	12.9	185	3.0	I	362±55
J1909+1102	283.642	149.98	10	185	26.4	C	206±31
J1910-0309	504.606	205.53	12.3	185	11.3	C	65±12
J1913-0440	825.936	89.39	12	185	103.9	C	445±165
J1916+0951	270.254	60.95	10.4	185	17.7	C	38±11
J1917+1353	194.631	94.54	6.5	185	53.4	C	174±37
J1921+1948	821.035	153.85	2.1	185	12.4	C	70±12
J1921+2153	1337.302	12.44	4.3	185	108.0	I	2112±49
J1922+2110	1077.924	217.09	2.2	185	25.5	C	67±15
J1932+1059	226.519	3.18	9.3	185	26.7	I	362±15
J1935+1616	358.738	158.52	6.6	185	10.2	I	106±9
J1939+2134	1.558	71.02	2.9	185	10.2	C	93±14
J1943-1237	972.429	28.92	5.7	185	12.5	I	68±8
J1946+1805	440.618	16.14	4.3	185	17.4	C	81±15
J2018+2839	557.953	14.20	1.2	185	16.7	I	561±41
J2046-0421	1546.938	35.80	14.6	185	11.0	I	34±7
J2053-7200	341.336	17.30	92.8	185	34.5	C	122±23
J2219+4754	538.469	43.50	103.1	185	17.3	I	871±58
J2253+1516	792.236	29.20	3.3	155	9.8	C	10±5
J2256-1024	2.295	13.78	2.7	155	4.2	C	67±20
J2346-0609	1181.463	22.50	4.1	185	9.0	C	8±4

1 Target offset from observation centre.

2 The mode of beamforming used. I: incoherent, where the detected powers of each tile are summed. C: coherent/tied-array, where the voltages of each tile are summed (after appropriate phase rotations to the pointing-direction) and then detected. For incoherent detections, flux density estimates are using the method outlined in Xue et al. (2017), whereas for coherent beam detections, they are estimated using the method described in § 4.2.

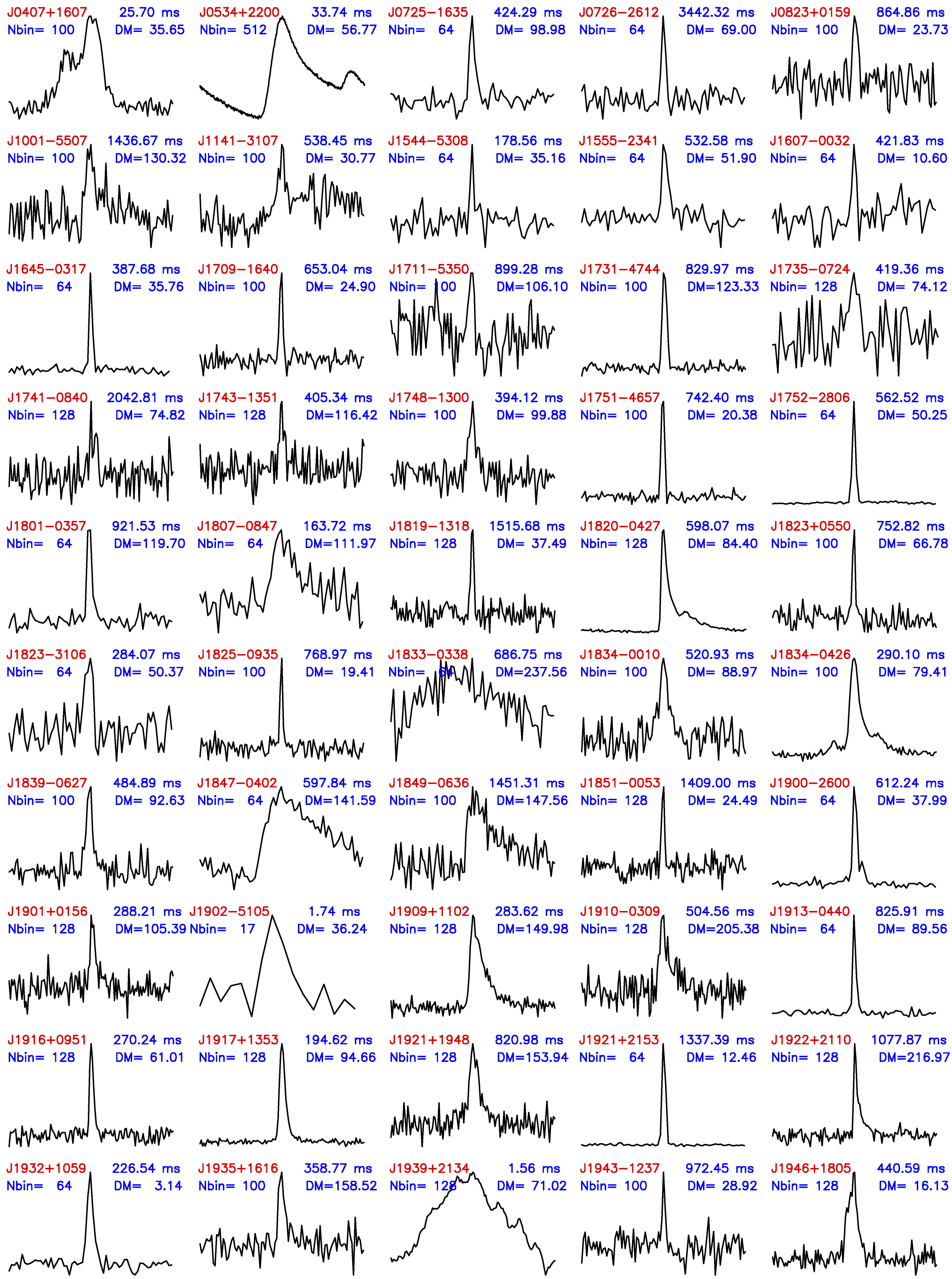


Figure 9. Integrated pulse profiles for 58 pulsars detected in observations of various non-SMART projects. The period, DM, and the number of phase bins are shown in each panel. Th majority of these detections were made in the 170-200 MHz band, while a few in the SMART survey band (140-170 MHz).

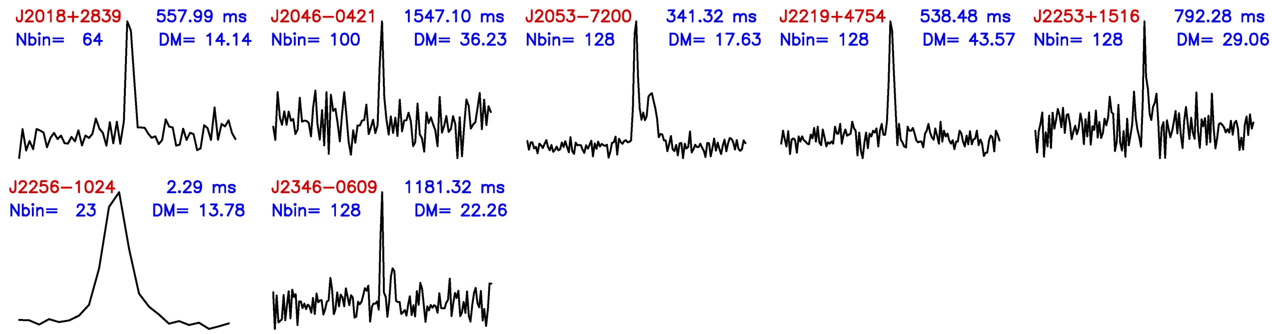


Figure 9. continued.